

GRAPHENE ELECTROMECHANICAL RESONATORS AND THEIR USE IN
THERMAL DETECTORS

by

ANDREW BLAIKIE

A DISSERTATION

Presented to the Department of Physics
and the Graduate School of the University of Oregon
in partial fulfillment of the requirements
for the degree of
Doctor of Philosophy

June 2020

DISSERTATION APPROVAL PAGE

Student: Andrew Blaikie

Title: Graphene electromechanical resonators for thermal detectors

This dissertation has been accepted and approved in partial fulfillment of the requirements for the Doctor of Philosophy degree in the Physics by:

Daniel Steck	Chairperson
Benjamín Alemán	Advisor
Raghuveer Parthasarathy	Core Member
Michael Kellman	Institutional Representative

and

Kate Mondloch	Interim Vice Provost and Dean of the Graduate School
---------------	--

Original approval signatures are on file with the University of Oregon Graduate School.

Degree awarded June 2020

© 2020 Andrew Blaikie
This work is licensed under a Creative Commons
Attribution-NonCommercial-NoDerivs (United States) License



DISSERTATION ABSTRACT

Andrew Blaikie

Doctor of Philosophy

Department of Physics

June 2020

Title: Graphene Electromechanical Resonators and their use in Thermal Detectors

In the quest to probe the nanoscale, new materials have been discovered. One of these materials is graphene, a sheet of carbon a single atom thick. An especially exciting application of graphene is its use in thermal detectors. These detectors sense broadband light by measuring an optical absorption induced temperature increase in a detecting material. Modern applications require that thermal detectors work at room temperature, while maintaining high speed and sensitivity, properties which are inherently limited by the heat capacity of the detector. To this end, graphene has generated interest because it has the lowest mass per unit area of any material, while also possessing extreme thermal stability and an unmatched spectral absorbance. Yet, due to its weakly temperature-dependent electrical resistivity, graphene has failed to challenge state-of-the-art thermal detectors at room temperature. Here, in a departure from conventional bolometric thermal detection, where the temperature-dependent electrical resistance serves as a readout for photodetection, we use a graphene nanoelectromechanical system to detect light via resonant sensing. In our approach, absorbed light heats and thermally tensions a suspended graphene resonator, thereby shifting its resonant frequency. Using the resonant frequency as a readout for photodetection, we achieve a room-temperature noise-equivalent power and bandwidth challenging the state of the art.

Despite great technological progress, scientific questions remain unanswered in graphene nanoelectromechanical systems, including the exact origin of their high mechanical dissipation, which could add noise in electromechanical sensing applications. Due to this high dissipation, the quality factor in suspended graphene, is orders of magnitude lower than in heavier bulk resonators. Here, we perform a large-scale study of the quality factor in suspended graphene drumheads to help further understand their mechanical dissipation properties. We find that the quality factor in graphene drumheads agrees with the predictions of a theory of dissipation dilution with a bending stiffness heavily modified by out-of-plane wrinkles. We find that Ga^+ ion irradiation increases in-plane stress and reduces wrinkling in graphene drumheads, improving the quality factor by a factor of 30.

This dissertation includes previously published and unpublished co-authored material.

CURRICULUM VITAE

NAME OF AUTHOR: Andrew Blaikie

GRADUATE AND UNDERGRADUATE SCHOOLS ATTENDED:

University of Oregon, Eugene, OR
College of Wooster, Wooster, OH

DEGREES AWARDED:

Expected Doctor of Philosophy, Physics, 2020, University of Oregon
Bachelor of Arts, Physics, Mathematics, 2013, College of Wooster

AREAS OF SPECIAL INTEREST:

Graphene, Nanomechanics, Optical Design, Nanofabrication, Detectors

PROFESSIONAL EXPERIENCE:

Research Assistant, University of Oregon, 2014-2020

Teaching Assistant, University of Oregon, 2013-2017

Teaching Assistant, Master's in Industrial Internship Program Photovoltaic and
Semiconductor Device Processing Track, 2016-2017, 2019

GRANTS, AWARDS, AND HONORS:

Doctoral Research Fellowship, University of Oregon, 2019-2020

National Science Foundation Graduate Research Fellowship Program Honorable
Mention, University of Oregon, 2014

Mahesh K. Garg Prize, The College of Wooster, 2013

Vivien Chan Prize, The College of Wooster, 2013

Arthur H. Compton Prize, The College of Wooster, 2013

PUBLICATIONS:

- Miller, D., Blaikie, A., Alemán, B. “Non-volatile rewritable frequency tuning of a nanoelectromechanical resonator using photoinduced doping” *Nano Letters*, (2020).
- Blaikie, A., Miller, D., Alemán, B. “A fast and sensitive room-temperature graphene nanomechanical bolometer”, *Nature Communications*, (2019).
- Ziegler, J., Klaiss, R., Blaikie, A., Miller, D., Horowitz, V., Alemán, B., “Deterministic Quantum Emitter Formation in Hexagonal Boron Nitride via Controlled Edge Creation”, *Nano Letters*, (2019).
- Miller, D., Blaikie, A., Carter, B., Alemán, B., “Engineering the Modal Shape of Graphene Nanoelectromechanical Systems Using Focused Ion Beam Milling”, *2018 IEEE 13th Nanotechnology Materials and Devices Conference*, (2018).
- Ziegler, J., Blaikie, A., Fathalizadeh, A., Miller, D., Yasin, F., Williams, K., Mohrhardt, J., McMorran, B., Zettl, A., Alemán, B. “Single-Photon Emitters in Boron Nitride Nanococoons”, *Nano Letters*, (2018).
- Blaikie, A., Saines, A. D., Schmitthenner, M., Lankford, M., Pasteur, R. D., Lindner, J. F., “Order and chaos in the rotation and revolution of two massive line segments.” *Physical Review E*, (2014).
- Blaikie, A., Abud, G., David, J. A., Pasteur, R. D. “NFL NCAA Football Prediction using Artificial Neural Networks.” *Proceedings of the Midstates Conference for Undergraduate Research in Computer Science and Mathematics*, (2011).

ACKNOWLEDGMENTS

My work in this dissertation, as well as my training as a scientist would not have been possible without the mentorship of Professor Benjamín Alemán. His passion, enthusiasm, endless creativity, and deep knowledge of nanoscale physics has been essential to help guide my academic career. I would also like to thank David Miller, who I collaborated with greatly. His work ethic, scientific rigor, and attention to detail was instrumental in producing many of the results in this work. I also collaborated with Josh Ziegler on quantum emitters, who I would like to thank for his get it done attitude. Additionally, I would like to thank Brittany Carter for her contributions in this area and her diligence. I would like to thank my lab and collaborators including Rudy Resch, Racheal Klaiss, Viva Horowitz, and Kara Zappitelli for scientific discussions and feedback, and also for making my work environment more enjoyable. Finally, I would like to thank my committee for their feedback and support during my research progress.

I would also like to acknowledge all of the pre-school, elementary, middle and high school teachers who helped me grow. I would also like to thank my undergraduate advisors including John Lindner and Drew Pasteur. Personally, I would like to thank my friends across many stages of life, who were always there for me. I would like to thank my brothers, Chris and Daniel, and my parents, Jean and Doug. Lastly, I would like to thank Carrie.

I would like to acknowledge the support by the University of Oregon and the National Science Foundation (NSF) under grant number DMR-1532225. The writing of this thesis was supported by the Doctoral Research Fellowship by the Graduate School at the University of Oregon.

For my parents and grandparents.

TABLE OF CONTENTS

Chapter	Page
I. INTRODUCTION	1
II. CONSTRUCTION AND OPERATION OF GRAPHENE RESONATORS	7
2.1. Fabrication of Suspended Graphene Drumheads	7
2.2. Focused Ion Beam Cutting of Graphene Trampolines.....	12
2.3. Operation of Graphene Electromechanical Resonators	13
III. ELECTROMECHANICS OF GRAPHENE DRUMHEADS.....	16
3.1. Mode Shape and Resonance Frequency for a Graphene Drumhead.....	16
3.2. Quality Factor in a Graphene Drumhead	21
3.3. Interaction with Electrostatic Gate.....	24
IV. GRAPHENE ELECTROMECHANICAL THERMAL DETECTORS	30
4.1. Introduction	30
4.2 Description of the GNB fabrication and mechanical measurements	34
4.3 Measurement of the noise-equivalent power	35
4.4 Modeling of the frequency responsivity to absorbed light.....	39
4.5 Measurement of the bandwidth.....	40
4.6 Discussion	44
4.7 Methods.....	47

Chapter	Page
V. DISSIPATION IN GRAPHENE DRUMHEADS	49
5.1. Introduction	49
5.2. Predictions of dissipation dilution for a Graphene Drumhead.....	51
5.3. Fabrication of Bilayer Graphene Drumheads.....	53
5.4. Characterization of Elastic Properties	56
5.5. Comparison to Dissipation Dilution Theory	59
5.6. Discussion	62
5.7. Methods.....	63
VI. CONCLUDING REMARKS AND FUTURE WORK	65
APPENDICES.....	67
A. Supporting Material for Chapter IV	67
B. Supporting Material for Chapter V.....	71
REFERENCES CITED.....	79

LIST OF FIGURES

Figure	Page
2.1. The fabrication procedure for the silicon support substrate	8
2.2. Semi-dry transfer of CVD grown graphene onto the silicon support substrate ...	10
2.3. Graphene nanomechanical resonators mounted in a dip-package	11
2.4. A focused ion beam cuts a graphene drumhead into a graphene trampoline	13
2.5. Optical measurement platform and apparatus	15
3.1. Drumhead membrane mode shapes for the first four resonance frequencies	21
3.2. Measurement of the resonance frequency for a graphene drumhead.....	23
3.3. Sketch of a GNB cross-section.....	24
3.4. The resonance frequency plotted vs. bias voltage.....	29
4.1. Design, images, and mechanical properties of graphene resonators.....	33
4.2. Frequency responsivity to absorbed light and frequency noise measurements ...	38
4.3. Modeling and bandwidth measurements of graphene resonators	43
4.4. SEM images gallery of all devices characterized.....	48
5.1. Analysis of the bilayer graphene drumhead dataset.....	55
5.2. Elastic properties of the bilayer graphene drumheads	58
5.3. Quality factor properties of bilayer graphene drumheads.....	61
B.1. Dilution factor analytic approximation plotted against the numerical solution ..	76
B.2. Elastic properties from 3-parameter fit.....	78

CHAPTER I

INTRODUCTION

Just after the turn of the 21st century, professors Novoselov and Geim discovered how to isolate a single layer atom thick layer of carbon at the University of Manchester¹. This material—graphene—is made from carbon atoms arranged in a honeycomb structure. Their method to isolate graphene, known as mechanical exfoliation, involved using scotch tape to peel off graphene from pyrolytic graphite. This technique was so effective and easy that this area of research grew extremely quickly. Labs were able to begin studying this two-dimensional material with little capital investment.

This widespread study of graphene was motivated by its remarkable material properties, which derive from its atomic thickness. Electric fields could not be screened inside the graphene, which allows an electrical conductivity that is strongly modulated by external electric fields. At that point, no metal or semimetal has been shown to exhibit any notable electric field effect¹. Graphene is also the strongest material ever measured², with a strength 200 times that of steel, while still maintaining flexibility. Furthermore, the band structure of graphene yields a flat ultra-broadband optical absorption^{3,4}, determined by the fine structure constant, from the ultra-violet to microwave.

However, the existence of graphene posed a problem. Experiments with graphene showed that it is a two-dimensional crystalline material, despite the fact that Mermin and Wagner concluded that perfect two-dimensional crystals could not exist with long range order⁵. The discrepancy was avoided by concluding that graphene was embedded in a larger three-dimensional structure supported by a bulk substrate. Wonderfully, just three years after the isolation of graphene, researchers demonstrated that freestanding graphene

sheets, are in fact, stable⁷. They concluded that random elastic deformations stabilized the two-dimensional crystalline structure, preserving the graphene. Due the excitement of its existence, extraordinary properties, and a plethora of potential applications, Novoselov and Geim received the 2010 Nobel Prize in Physics.

As one of its promising applications, researchers have exploited the extraordinary properties of graphene to detect broadband light⁸. An especially exciting graphene light detector is a graphene thermal detector, where absorbed light is detected by the measuring the absorption induced temperature rise in a graphene sheet. The primary benefit of a thermal detector is its ability to detect light deep into the infrared, a notoriously difficult region of light to see. The unmatched ability of graphene to absorb any color of light would make it an excellent ultra-broadband thermal detector. More promising still, graphene's extremely low mass-per-unit-area allows it to heat up or cool down quickly. With graphene's unique properties, a graphene thermal detector could detect broadband light with an ultrafast response.

Several designs have been explored to build a graphene thermal detector. A promising design is a graphene hot electron bolometer⁹⁻¹³, where at cryogenic temperatures, a weak electron-phonon interaction generates a thermally insulated electron gas with a low electronic heat capacity. This electron gas temperature can be readout electrically. However, due to the cryogenic temperatures needed, these designs lack portability. Another interesting design exploits the electric field effect in graphene to detect the electric charge generated in nearby optically active materials, such as quantum dots¹⁴ or pyroelectric crystals¹⁵. However, these devices merely use the graphene as a

transducer for the nearby optically active material, and thereby cannot directly exploit the low mass and broadband absorption of graphene.

Despite the promise, previous research on freestanding graphene based thermal detectors have failed to produce a competitive technology when operating at ambient temperatures. The primary challenge is that any thermal detector must possess a large thermal responsivity, where some measurable aspect of the material reversibly and strongly changes with rising temperatures. This thermal responsivity is typically achieved with a temperature-dependent electrical resistance. Thermal detectors that use a temperature-dependent electrical resistance for the thermal responsivity are called a bolometer. For industry standard materials such as vanadium dioxide, this temperature-dependent electrical resistance is typically 2 - 4 % K^{-1} (ref. ¹⁶). Unfortunately, graphene has an incredibly weak temperature-dependent electrical resistance¹⁷, 0.15 % K^{-1} , frustrating advancements in ambient temperature graphene bolometry.

The lack of advancements in ambient temperature graphene-based thermal detection motivate new approaches. Fortunately, graphene has a suite of exciting mechanical properties. In 2008, researchers showed that freestanding graphene has a strong mechanical resonance, where a freestanding graphene sheet resonates when vibrated at a particular frequency¹⁸. These electrically actuated suspended graphene sheets (called graphene electromechanical resonators) are the thinnest mechanical resonator ever created. Because of their atomic thickness, and thus ultra-low mass, the resonance frequency of these suspended graphene sheet becomes very sensitive to any changes in its surrounding environment. Consequently, graphene electromechanical resonators have incredible sensitivity to charge¹⁸, mass¹⁹, force²⁰, and pressure²¹. More

exciting still, graphene electromechanical resonators have remarkable thermal properties. Freestanding graphene is thermally stable up to at least 2600 K (ref. ²²) and graphene electromechanical resonators have been measured even when operating at 1200 C (ref. ²³). Fortunately, this resonant frequency changes with temperature, at 2% K⁻¹ (ref. ²⁴), in line with the responsivity with other industry standard materials, and is much higher than graphene's temperature-dependent electrical resistance¹⁷ at 0.15 % K⁻¹.

In this dissertation, we show how to construct and operate an ambient temperature graphene thermal detector with record speed and sensitivity. This is accomplished by exploiting the interaction between mechanical motion and thermal heating. We call this type of graphene thermal detector a graphene nanomechanical bolometer. It is created by stretching a sheet of freestanding graphene over a hole etched into a silicon chip. This graphene electromechanical resonator vibrates at a known consistent resonance frequency. That is, until it absorbs light. When exposed to even tiny amounts of light the graphene resonator rapidly heats up (in as fast as one millionth of a second). This heat tightens the suspended graphene sheet, changing the resonance frequency. By tracking changes in the resonance frequency, we can determine the precise amount of light hitting the graphene. In this way, we turn a graphene electromechanical resonator into a thermal detector.

Despite all of the technological progress made with graphene electromechanical resonators, scientific questions still remain about the physical dissipation mechanisms, which could affect the noise in graphene sensors, such as the graphene nanomechanical bolometer. Based off the mechanical strength, thickness, and elastic modulus of freestanding graphene sheets, typical graphene electromechanical resonators have a

mechanical dissipation hundreds of times larger than expected²⁵⁻²⁷. Researchers have only noted trends in dissipation, such as a linear dependence with size²⁷, but have not fully explained why dissipation is low.

This dissertation describes experiments undertaken to explore the dissipation and quality factor in graphene electromechanical resonators. We use a theory called dissipation dilution to model the quality factor, which assumes that energy is primarily stored in elongation and that bending losses dominate the dissipation. Our results indicate that elastic deformations (wrinkles) in suspended graphene sheets greatly increase the bending stiffness of the graphene, which increases the bending losses, which explains their higher dissipation. Furthermore, we find that exposing the graphene sheet to large amounts of Ga⁺ ion irradiation is able to apply enough stress to reduce these wrinkles and thus reduce the mechanical dissipation.

This dissertation is laid out in 6 chapters. In chapter 2, we describe how to construct and operate graphene electromechanical resonators. We describe the multi-step photolithography procedure used in order to construct the silicon supporting substrate. Next, we show how a semi-dry transfer of chemical vapor deposition grown graphene is used to suspend graphene over circularly etched holes to make graphene drumheads. Then we show how the graphene resonators can be cut with a tightly focused Ga⁺ ion beam to construct graphene trampoline resonators, which make the most sensitive graphene thermal detectors. We describe how to electronically actuate these devices with a capacitive back-gate. Finally, we show how to readout their motion with Fabry-Perot interferometry.

In chapter 3, we describe the relevant physics needed to understand the electromechanics of graphene resonators. First, we begin by describing the role of bending energy and elastic energy when determining the mode shape and resonance frequencies in graphene circular drumheads. Next we define the quality factor of the resonance and show how it relates to dissipation. Then we describe in detail the capacitive interaction with the biased back-gate. The capacitive back-gate is inherently nonlinear, can lead to both frequency tuning and the extraction of the stress, modulus, and mass density of the graphene sheet, by sweeping the voltage.

In chapter 4, we describe the graphene nanomechanical bolometer and the experiments performed. We show that the thermal detector can achieve sensitivities comparable to the state-of-the-art microbolometers with record bandwidths, due to graphene's low heat capacity. We also describe the differences between different types of graphene electromechanical resonators in speed and sensitivity.

In chapter 5, we discuss our experiments on the role of wrinkles in the dissipation in graphene drumheads and describe how graphene resonators can be engineered to have low dissipation. The wrinkles in freestanding graphene greatly increase the dissipation in graphene electromechanical resonators. We also show how Ga^+ irradiation can dramatically increase the quality factor in graphene drumheads. These results pave the way to more exciting applications in graphene electromechanical resonators.

We conclude this exploration of graphene electromechanical resonators and their use in thermal detectors in chapter 6. We summarize the findings of this dissertation research and describe these results in the context of graphene research.

CHAPTER II

CONSTRUCTION OF GRAPHENE RESONATORS

In this chapter, I provide an overview of how graphene resonators are fabricated, shaped, actuated, and transduced. I discuss the multi-step photolithography procedure for how the silicon supporting substrate is prepared and discuss how the graphene is transferred onto the substrate. Finally, I describe how the graphene resonators are actuated with a capacitive force and transduced with optical interferometry.

2.1. Fabrication of Suspended Graphene Drumheads

The graphene nanomechanical resonators fabricated for this work are made by suspending a monolayer or bilayer sheet of chemical vapor deposition grown graphene over a lithographically patterned hole etched into SiO₂ grown on a Si⁺⁺ wafer. To prepare the Si⁺⁺ supporting substrate we used standard semiconductor processes which is outlined in Figures 2.1a-k. We began by growing 1 μm of wet thermal oxide on ~ 5 x 5 mm degenerately doped Si⁺⁺ wafers at 1100 C for ~ 2 hours in a tube furnace. To ensure that the oxide did not have any scratches that could lead to an electrical short, the wafers were baked in in 1100 C tube furnace with flowing dry O₂ for 30 minutes. To expose the backside of the Si⁺⁺, the topside SiO₂ was covered with 2 layers of AZ1512 photoresist and the substrate was etched in HF 5:1 BOE until the backside oxide was removed.

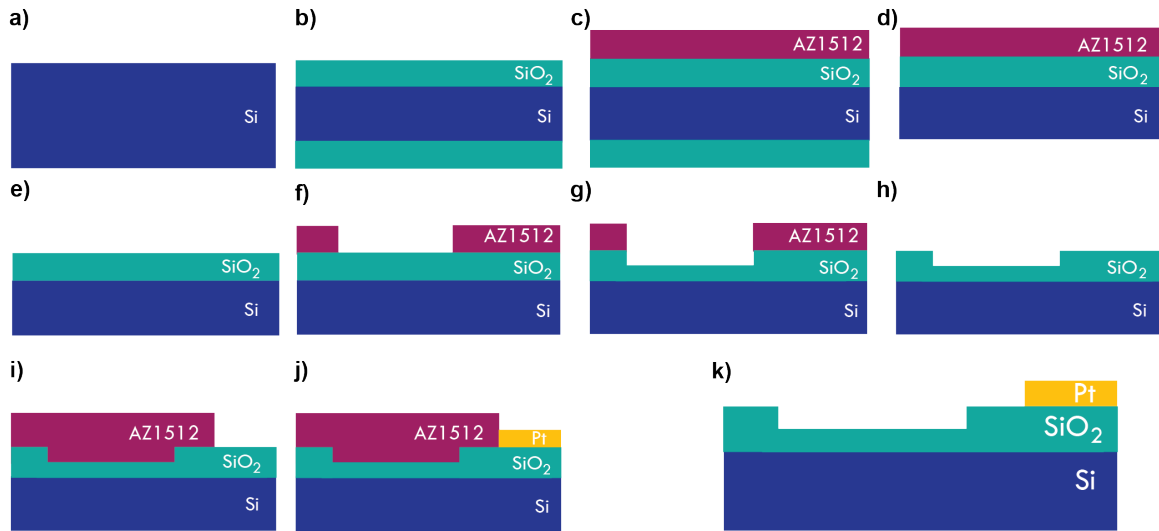


Figure 2.1: The fabrication procedure for the silicon support substrate. (a) Clean a Si⁺⁺ 5x5 mm wafer. (b) Grow 1 μm of wet oxide on the wafer in a 1100 C tube furnace. (c) Spin on two layers of AZ1512 photoresist at 4000 rpm. (d) Etch the oxide on backside of the wafer in HF 5:1 BOE. (e) Remove the photoresist in acetone and clean the wafer. (f) Pattern AZ1512 photoresist with a direct write photolithography system to expose circular holes (g) Use a dry inductively coupled etch of argon and CHF₃ to etch 600 nm of oxide with vertical sidewalls. (h) Remove the photoresist in acetone and clean the wafer. (i) Pattern AZ1512 photoresist with direct write photolithography system to expose an area for metal electrodes. (j) Evaporate platinum with a titanium adhesion layer to create electrodes. (k) Remove the photoresist with sonication in acetone. Clean the finished the silicon support substrate.

Next, we patterned 6-8 μm diameter holes with AZ1512 photoresist and a direct write laser photolithography system. The wafers were sonicated in acetone for 10 minutes to remove organic residue, which was followed by an IPA rinse. Any water residue was

next removed by placing the wafers on a hot plate at 400 C for 10 minutes. Next, to ensure a hydrophobic surface, the wafers were exposed to an opened vile of HMDS in an enclosed volume (~ 1 liter) for 1 hour. A MicroChem AZ1512 resist was spun on at 4000 rpm for 30 seconds on a Laurell Technologies spin coater. The photoresist was then soft baked at 105 C for 2 minutes to remove all of the solvent from the photoresist. The photoresist was exposed with a direct write photolithography system with an exposure dose of 380 mJ cm⁻² using a 1 μm spot size objective. The resist was developed in an MicroChem 300 MIF TMAH developer for 1 minute with gentile agitation.

We etched 600 nm deep into the exposed SiO₂ with a dry inductively coupled plasma etch using CHF₃ and Ar which etched at a rate of ~75 nm per minute. To keep etch rates constant, we kept the plasma exposure to cycles under 2-minute intervals. By leaving 400 nm of oxide intact, any collapsed graphene could not cause a short between the suspended graphene and the Si⁺⁺. The photoresist was then removed with an acetone sonication for 10 minutes.

We then patterned metal electrodes using another AZ1512 direct write photolithography step. The procedure to prepare the wafer and pattern the photoresist was the same as described previously. We then evaporated 5/50 nm Ti/Pt using electron beam evaporation. We removed the photoresist by first soaking the wafers in acetone for 2 hours. Then, we sonicated the acetone for 10 minutes, which removed the photoresist and left the metal electrodes intact. Altogether, this multi-step photolithography process was sufficient to make the supporting substrates that were ready for a graphene transfer.

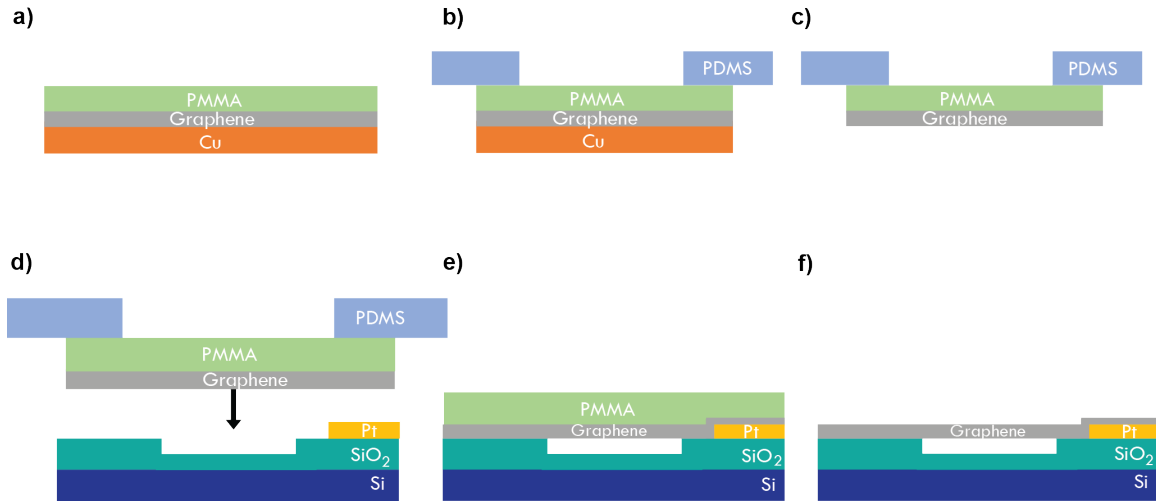


Figure 2.2: Semi-dry transfer of CVD grown graphene onto the silicon support substrate. (a) Spin on PMMA resist onto the graphene side of the graphene grown on copper foil (b) Place a PDMS with a large hole removed onto the PMMA. This step adds significant rigidity to the foil. (c) Etch the copper by floating the foil in a bath of ammonium persulphate. (d) Using tweezers place the graphene onto the silicon support substrate at 155 C. (e) Peel off the PDMS layer and leave the graphene/PMMA on the wafer at 155 C for 16 hours. (f) Remove the PMMA layer in a tube furnace flowing H_2 and Ar for 3 hours.

To transfer the graphene onto the supporting substrate we used a semi-dry graphene transfer process outlined in Figure 2.2a-f. We used commercial CVD graphene grown on copper foil (Graphenea) for the transfer. Any graphene on the backside of the foil was removed with an oxygen plasma etch. Next, a 3-micron thick layer of PMMA A11 resist was spun onto the graphene side of the copper foil. Then, a 1 mm thick piece of PDMS with a ~ 1 cm diameter hole punched through the middle of it was placed on top of the Graphene/Cu stack. A thin plastic backing was left on the PDMS to increase the

rigidity of the film. Next, the stack was placed copper side down in a solution of ammonium persulphate (40 mg/ml) to etch away the copper. The relatively rigid PDMS/PMMA/Gr stack was picked up with tweezers and placed in three sequential water baths and then dried in air. Concurrently, the target supporting substrate was prepared by cleaning it in oxygen plasma before placing it on a hot plate at 155 C.

The now dry PDMS/PMMA/Graphene stack was placed on top of the hot substrate with the through hole covering the entirety of the active area of the chip. The substrate was left on this 155 C hot plate for ~16 hours to improve adhesion between the graphene and the SiO₂. The PDMS was then peeled away and the PMMA was removed in a tube furnace, by flowing Ar and H₂ at 350 C for 3 hours. Sharp tweezers were used to scratch any graphene off the perimeter of the substrate to prevent shorting to the Si⁺⁺ gate.

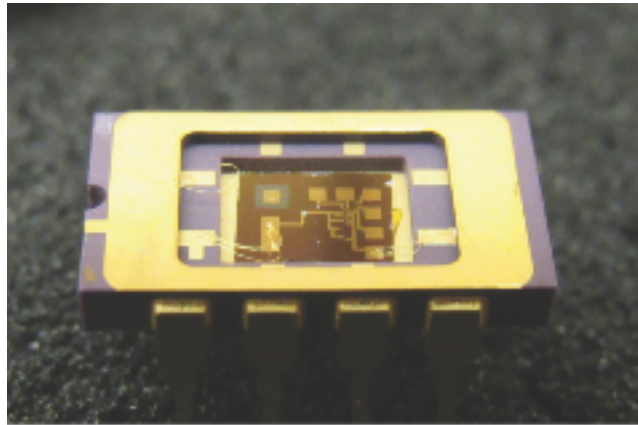


Figure 2.3: Graphene nanomechanical resonators mounted in a dip-package. Photograph of graphene NEMS device mounted in the dip package.

In order to mount the substrate into a vacuum chamber with electrical actuation the substrate was placed in a dip package. The substrate was glued to the dip package

with conductive epoxy. This allowed the backside Si^{++} to be electrically addressed. The topside platinum electrodes were wire bonded to the top of the dip package. This system is shown in a photograph of one such device is shown in Figure 2.3.

2.2. Focused Ion Beam Cutting of Graphene Trampolines

We shaped some of the graphene drumheads into graphene trampolines with a focused ion beam, which is shown in a schematic in Figure 2.4a. FIB shaping was performed in a FEI Helios 600i SEM-FIB with a focused Ga^+ ion source. The ion-beam current and voltage were 1.1 pA and 30 kV, respectively. To fabricate a trampoline, four circle line cuts were used to cut into a graphene drumhead using a single beam pass and a dwell time of 1 ms, which was enough to etch completely through the suspended graphene sheet. The high tension in the graphene sheet causes the graphene inside the circular cut to pull away from the trampoline resonator and collapse into the cavity. The FIB fabrication technique has a yield of near 100%, with device failures typically due to holes or other defects present in the graphene prior to milling. Although the FIB milling likely induces additional disorder in the graphene sheet, it still maintains its electrical, mechanical, and thermal properties.

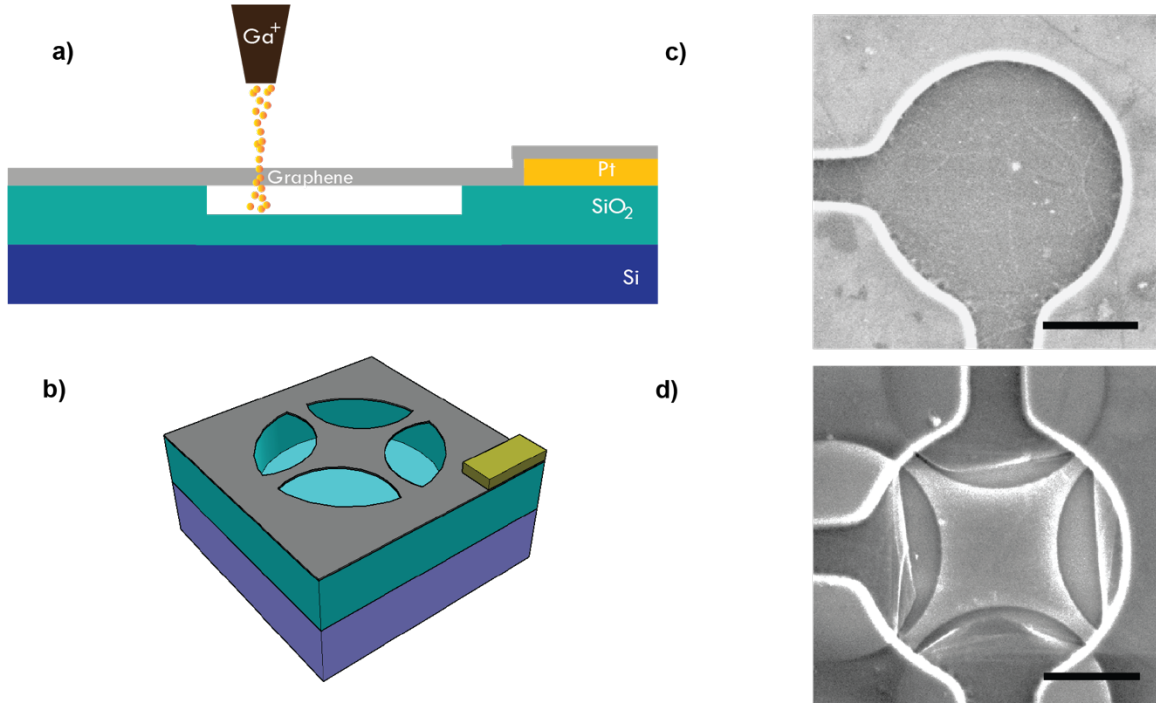


Figure 2.4: A focused ion beam cuts a graphene drumhead into a graphene trampoline. (a) Schematic of the focused Ga⁺ beam used to cut into the graphene drumhead. (b) Schematic of the fully cut suspended graphene trampoline. (c) Scanning electron microscope image of a graphene drumhead. (d) Scanning electron microscope image of a graphene drumhead.

2.3. Operation of Graphene Electromechanical Resonators

The graphene nanomechanical resonators interact strongly with an electrostatic back-gate. We apply a bias voltage with both a DC offset term and a rf term so that the total voltage is $V = V_{\text{DC}} + V_{\text{AC}} \sin(\omega t)$. In our system, V_{DC} is typically much larger than V_{AC} so we can write the electrostatic force with an offset force term and an oscillating force term at frequency ω ,

$$F = \frac{1}{2} \left(\frac{dC}{dz} \right) V^2 \approx -\frac{1}{2} \left(\frac{dC}{dz} \right) V_{\text{DC}}^2 - \left(\frac{dC}{dz} \right) V_{\text{DC}} V_{\text{AC}} \sin(\omega t) \quad (2.1)$$

Therefore, the driving force at frequency ω is proportional to both the DC offset voltage and the RF voltage, $F_\omega \propto V_{\text{DC}}V_{\text{AC}}$. In addition to supplying the driving force to actuate motion in our graphene resonators, the electrostatic gate provides a way to tune the resonance frequency of the device which is discussed more in chapter 3.

The motion of the graphene mechanical resonators was transduced with optical interferometry and lock-in amplification, which can be seen as a schematic in Figure 2.5a. A 633 nm probe laser ($< 1 \mu\text{W}$) was focused down onto the graphene resonators through a viewport in the vacuum chamber using a 40x, 0.6 NA objective. A low-finesse Fabry-Perot cavity, formed between the Si^{++} and the graphene, applies a small modulation to the reflected light as the resonator vibrates. We used a polarizing beam splitter and a quarter waveplate to split the reflected light from the incident beam. The intensity of the reflected beam was converted to a voltage using a silicon avalanche photodiode before being fed into a lock-in amplifier referenced to the applied V_{AC} electrical drive signal. The mode shape of the graphene drums²⁸ could be visualized by scanning the 633 nm probe laser across the device using a fast steering mirror with diffraction limited resolution. All measurements were done under vacuum at less than 10^{-5} Torr to minimize air damping. The vacuum chamber used is pictured in Figure 2.5b.

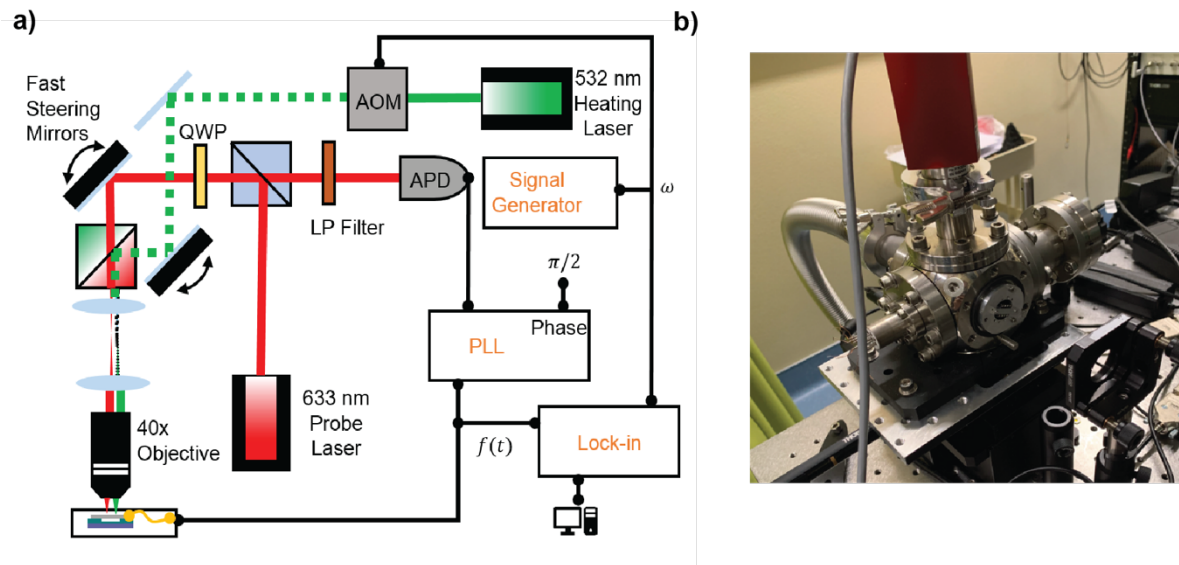


Figure 2.5. Optical measurement platform and apparatus. (a) Sketch of the optical interferometer setup used to measure the motion of and apply heating radiation to the suspended graphene. (b) Vacuum chamber that the graphene trampolines were placed in.

CHAPTER III
ELECTROMECHANICS OF GRAPHENE DRUMHEADS

In this chapter, I provide an overview of the equations of motion and solutions for a vibrating graphene drumhead. I also discuss how an electrostatic back-gate is used to both actuate motion and tune the resonance frequency. The electrostatic force applied by this gate is inherently nonlinear, which allows for the calculation of the initial in-plane stress, the in-plane elastic modulus, and mass-per-unit-area of the graphene drumheads.

3.1. Mode Shape and Resonance Frequency for a Graphene Drumhead

We begin by defining all of the relevant energy terms in a vibrating graphene drumhead. The kinetic energy of the membrane is then given by the integral

$$T = \frac{\rho}{2} \int dA (\dot{u})^2, \quad (3.1)$$

where ρ is the mass per unit area of the drumhead, $\int dA$ is the area integral over the suspended region of the drumhead, $\dot{u} = du/dt$ is the time derivative of the out-of-plane displacement, and $u(\vec{r}, t)$ gives the out-of-plane displacement of the graphene membrane.

The vibrating drumhead also has potential energy components. The potential energy due to in-plane stress is conservative, and can be calculated from the gradient of the out-of-plane displacement

$$U_\sigma = \int dA \frac{\sigma}{2} (\nabla u)^2, \quad (3.2)$$

where σ is the initial in-plane stress. There is also a dissipative bending potential energy which has an energy that can be calculated from the Laplacian of the out of plane displacement

$$U_\kappa = \int dA \frac{\kappa}{2} (\nabla^2 u)^2, \quad (3.3)$$

where κ is the bending stiffness. There also exist higher-order nonlinear potential energy terms associated with deformation induced stress, also known as self-stress. However, we actuate the graphene drumheads with small displacements so that these terms may be ignored for now.

We find the equations of motion with the Lagrangian approach. The Lagrangian of the vibrating graphene drumhead has the form

$$\mathcal{L} = \int dA \frac{\rho}{2} (\dot{u})^2 - \int dA \frac{\kappa}{2} (\nabla^2 u)^2 - \int dA \frac{\sigma}{2} (\nabla u)^2, \quad (3.4)$$

$$\mathcal{L} = \int dA \left(\frac{\rho}{2} (\dot{u})^2 - \frac{\kappa}{2} (\nabla^2 u)^2 - \frac{\sigma}{2} (\nabla u)^2 \right), \quad (3.5)$$

The Euler-Lagrange equation that minimizes the action of this integral is

$$\frac{d}{dt} \left(\frac{\partial \mathcal{L}}{\partial \dot{u}} \right) + \nabla \frac{\partial \mathcal{L}}{\partial (\nabla u)} - \nabla^2 \left(\frac{\partial \mathcal{L}}{\partial (\nabla^2 u)} \right) = 0, \quad (3.6)$$

which gives the equation of motion

$$\nabla^2 (\kappa \nabla^2 u) - \sigma \nabla^2 u + \rho \ddot{u} = 0. \quad (3.7)$$

This is the Poisson Kirchhoff equation of motion for a vibrating plate. To find a solution to this equation, we use separation of variables to let $u(\vec{r}, t) = u(\vec{r}) \sin(\omega_0 t)$, to separate the time varying component from the mode shape $u(\vec{r})$. For mathematical simplicity, we also assume that the bending stiffness κ and the in-plane stress σ are constant over the membrane. Plugging into Equation 3.7, we simplify the equation to be

$$\kappa \nabla^4 \mathbf{u} - \sigma \nabla^2 \mathbf{u} - \omega_0^2 \rho \mathbf{u} = 0. \quad (3.8)$$

This equation of motion has the general solution²⁹ in polar coordinates

$$\mathbf{u}(r, \theta) = (A_n J_n(\alpha r) + B_n I_n(\beta r)) \cos(n\theta + \phi_n), \quad (3.9)$$

$$\alpha^2 = \frac{\sigma}{2\kappa} \left(\left(1 + \frac{4\omega_0 \rho \kappa}{\sigma^2} \right)^{\frac{1}{2}} - 1 \right), \quad (3.10)$$

$$\beta^2 = \frac{\sigma}{2\kappa} \left(\left(1 + \frac{4\omega_0 \rho \kappa}{\sigma^2} \right)^{\frac{1}{2}} + 1 \right), \quad (3.11)$$

where J_n is the Bessel function of the first kind, I_n is the modified Bessel function of the first kind, and A_n , B_n , and ϕ_n are constants determined by boundary and initial conditions. For a clamped circular plate of radius a , (which models a graphene drumhead), the mode shape must obey the boundary conditions $\nabla \mathbf{u}(r = a, \theta) = 0$ and $\mathbf{u}(r = a, \theta) = 0$. For these boundary conditions, the solution²⁹ has the mode shape

$$\mathbf{u}(r, \theta) = x \left(J_n \left(\alpha \frac{r}{a} \right) - \frac{J_n(\alpha)}{I_n(\beta)} I_n \left(\beta \frac{r}{a} \right) \right) \cos(n\theta) \sin(\omega t), \quad (3.12)$$

where J_n is the Bessel function of the first kind, I_n is the modified Bessel function of the first kind, a is the membrane radius, and x is the amplitude of oscillation (there also exists a degenerate solution with $\sin(n\theta)$ in place of $\cos(n\theta)$ for $n > 1$). The parameters α and β are determined from the coupled equations

$$\alpha \frac{J_{n+1}(\alpha)}{J_n(\alpha)} + \beta \frac{I_{n+1}(\beta)}{I_n(\beta)} = 0, \quad (3.13)$$

$$\beta^2 - \alpha^2 = \frac{\sigma a^2}{\kappa} \stackrel{\text{def}}{=} \frac{1}{\lambda^2}, \quad (3.14)$$

where λ is defined as the dilution parameter. The first term in Equation 3.12, proportional to $J_n \left(\alpha \frac{r}{a} \right)$, predominantly describes the mode shape away from the clamping region, and

the second term, proportional to $I_0\left(\beta\frac{r}{a}\right)$, adjusts the mode shape to account for the clamped edges. The resonance frequency of the solution is given by,

$$\omega_0 = \frac{\alpha}{a^2} \sqrt{\frac{\sigma a^2}{\rho} + \frac{\kappa a^2}{\rho}}. \quad (3.15)$$

This mode shape and resonance frequency describes the solution to a clamped circular plate.

However, in the limit of a plate with ultra-low bending stiffness the solution can be simplified to recover the commonly used drumhead mode shape for a thin membrane. Typically, $\kappa \propto h^3$, where h is the thickness of the membrane, which in the case of graphene, is less than a nanometer. Given the atomic thickness of a graphene sheet, we discuss this simplification. Namely, we make the assumption that the in-plane stress energy is much larger than the bending stiffness, $\sigma a^2 \gg \kappa$. First, this allows us to make the approximation, $\beta \gg 1$, which predicts, $\frac{I_{n+1}(\beta)}{I_n(\beta)} \rightarrow 1$, which then allows us to simplify Equation 3.13 to

$$J_n(\alpha) + \frac{\alpha}{\beta} J_{n+1}(\alpha) \approx 0. \quad (3.16)$$

Moreover, since $\beta \gg 1$, we can approximate α is the root of the equation $J_n(\alpha) \approx 0$ according to Equation 3.16. This allows us to write the mode shape as

$$u(r, \theta) = x \left(J_n\left(\alpha\frac{r}{a}\right) + \frac{\alpha J_{n+1}(\alpha)}{\beta I_n(\beta)} I_n\left(\beta\frac{r}{a}\right) \right) \cos(n\theta) \quad (3.17)$$

Next, we can drop the term proportional to $1/\beta$ in Equation 3.17 to get the simplified mode shape,

$$u(r, \theta) \approx A J_n\left(\alpha\frac{r}{a}\right) \cos(n\theta), \quad (3.18)$$

where we note that there also exists a degenerate solution with $\sin(n\theta)$ in place of $\cos(n\theta)$ for $n > 1$. The first four mode shapes are shown in Figure 3.1a-d. This is the well-known drumhead solution to the membrane equation

$$\sigma \nabla^2 u = \rho \frac{\partial^2 u}{\partial t^2}, \quad (3.20)$$

with circular clamping conditions. Furthermore, the resonance frequency approaches that of the membrane approximation

$$f_0 \approx \frac{\alpha}{2\pi a} \sqrt{\frac{\sigma}{\rho}}. \quad (3.21)$$

Typically, graphene drumheads are described with the membrane approximation^{28,30}, and, in most cases this is a valid assumption. Quantitatively, the membrane approximation is valid in the regime where the dilution parameter is small, $\lambda = \sqrt{\frac{\kappa}{\sigma a^2}} \ll 1$, which characterizes the energy stored in bending relative to in-plane stress. Despite measurements³¹ finding that the bending stiffness is orders of magnitude higher than expected, graphene drumheads are well approximated by the membrane equation. Measurements found values of $\kappa_1 \sim 5$ keV (ref. ³¹), $T \sim 0.05$ N m⁻¹ (ref. ³⁰), and $a \sim 5 \times 10^{-5}$ m (ref. ²⁷), which predicts $\lambda = \sqrt{\frac{\kappa_1}{\sigma a^2}} \sim 0.025 \ll 1$, which is consistent with this approximation.

Yet, there are situations when this approximation breaks down and the full solution that takes into account bending energy is needed. We will show that the bending at the clamped edges cannot be ignored in order to describe dissipation in graphene electromechanical resonators. Furthermore, we show that the bending stiffness limits how sensitive a graphene nanomechanical thermal detector can be, whereas the membrane

approximation predicts an infinite sensitivity for a graphene drumhead with no initial in-plane stress. Therefore, the plate solutions given in Equations 3.12, 3.13, and 3.14, are necessary to describe the physics of a vibrating graphene drumhead.

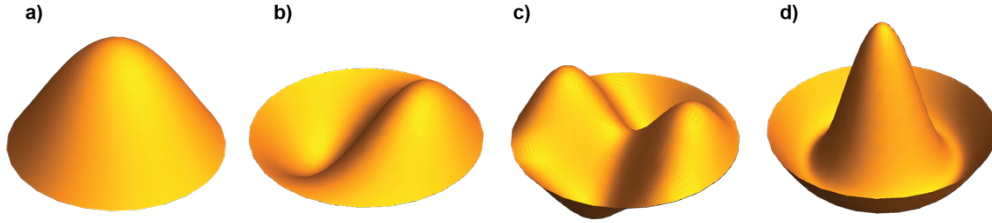


Figure 3.1: Drumhead membrane mode shapes for the first four resonance frequencies. (a) The fundamental drumhead mode, u_{10} . (b) The degenerate first fundamental mode, u_{11} . (c) The degenerate u_{12} mode. (d) The non-degenerate u_{20} mode.

3.2. Quality Factor in a Graphene Drumhead

When a periodic force acting on a suspended graphene sheet is applied near the resonance frequency of the resonator its amplitude of motion increases dramatically. The quality factor, Q , characterizes the strength of this amplitude enhancement.

Quantitatively, the quality factor is defined as the ratio of the resonance frequency to the full-width-half-max of the resonant amplitude, $Q = f_0/\Delta f$.

In graphene NEMS, $Q \sim 10^2$ (ref. ²⁷), and in the limit where $Q \gg 1$, the resonator amplitude of motion can be approximated as a damped-driven-harmonic oscillator³² according to

$$\frac{d^2x}{dt^2} + 2\beta \frac{dx}{dt} + \omega_0^2 x = F \cos(\omega t), \quad (3.22)$$

where F is the driving force amplitude, $\omega = 2\pi f$, and $\omega_0 = 2\pi f_0$ and β is an experimentally determined damping constant.

For the graphene drumheads we fabricate, we typically find a quality factor²⁷, $Q > 50$, the amplitude and phase can be modeled by the equations,

$$x = \frac{F_m}{\sqrt{(\omega_0^2 - \omega^2)^2 + 4\omega^2\beta^2}}, \quad (3.23)$$

$$\phi = \arctan\left(\frac{2\beta\omega_0}{\omega_0^2 - \omega^2}\right), \quad (3.24)$$

where x is the amplitude and ϕ is the phase between the amplitude and the driving force.

We measure the resonance frequency for an 8 μm diameter graphene drumhead in Figure 3.2a by sweeping the amplitude vs. driving frequency, where we fit a quality factor of $Q \sim 720$. We confirm that the fundamental mode is measured by scanning the scanning the laser interferometer across the drumhead and measure the amplitude as seen in Figure 3.2b. The reflected beam was measured using a silicon avalanche photodiode and referenced to the applied V_{AC} drive signal with a lock-in amplifier.

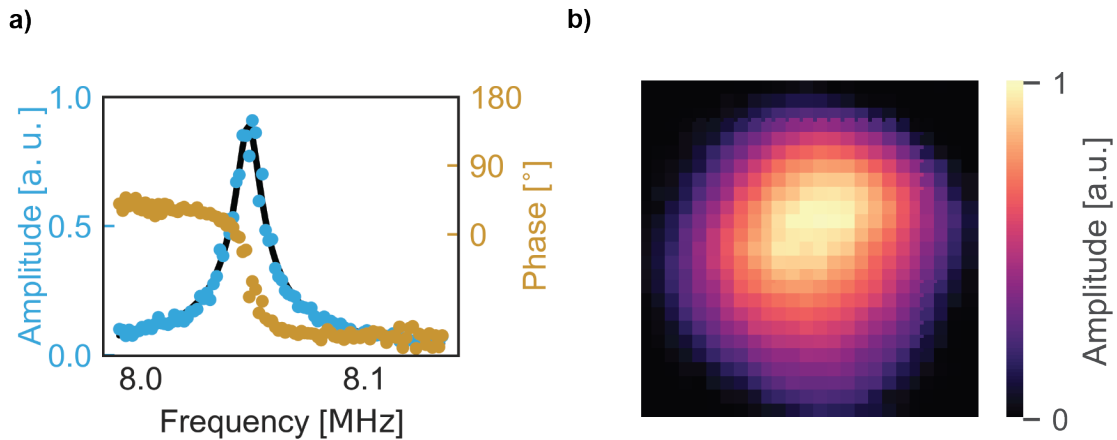


Figure 3.2: Measurement of the resonance frequency for a graphene drumhead. (a)

The amplitude vs. driving frequency curve for an 8 μm diameter graphene drumhead near the fundamental mode resonance. (b) The mechanical mode shape as the drumhead is driven on resonance. A diffraction limited laser was scanned across the drumhead to produce this curve. We plot the amplitude of the reflected interferometric signal at the driving frequency vs. position to create this mode map.

3.3. Interaction with Electrostatic Gate

The graphene drumhead feels a strong electrostatic force when a bias voltage is applied to the graphene – Si^{++} system. This force pulls the graphene down towards the substrate which tightens the drumhead. Therefore, a large V_{DC} can be used to tune the resonance frequency by changing the tension. In this section, we analyze the capacitive energy term in the Lagrangian to understand how it can be used to tune the resonance frequency.

To understand how this back-gate interacts with the graphene drumhead, we first define the capacitance of the graphene– SiO_2 – Si^{++} system in more detail, which is shown

in Figure 3.3. The capacitance of the system can be written as the sum of capacitors in parallel,

$$\frac{1}{C} = \frac{d_v}{\epsilon_0 A} + \frac{d_o}{\epsilon_0 \epsilon_r A} = \frac{d}{\epsilon_0 A}, \quad (3.25)$$

where A is the area of the drumhead and $\epsilon_r = 3.9$ is the relative permittivity of SiO_2 , d_v is the distance between the suspended graphene and oxide (which is in vacuum), and d_o is the thickness of the oxide between the Si^{++} and vacuum. These distances d_v and d_o are measured with atomic force microscopy. The effective distance can be written as $d = d_v + \frac{d_o}{\epsilon_r}$. The electrostatic back gate has a capacitive energy of

$$E_c = \frac{\epsilon_0 V_{DC}^2}{2} \int \frac{dA}{d - u}. \quad (3.26)$$

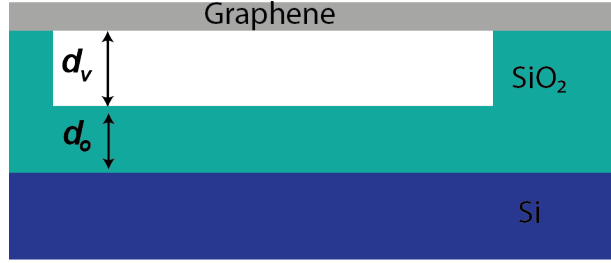


Figure 3.3: Sketch of a GNB cross-section. d_v is the distance between the suspended graphene and the SiO_2 . d_o is the oxide layer thickness protecting the silicon back gate.

The graphene membrane will undergo a large static deformation in the presence of this force. Therefore, we now need to include the nonlinear self-stress energy term.

This self-strain term and can be written as the integral³⁰

$$U_Y = \frac{C}{16} \left(\frac{\int dA (\nabla u)^2}{\int dA} \right) \int dA (\nabla u)^2 \quad (3.27)$$

where $C = \frac{Y}{1-\nu^2}$, and Y is the in-plane elastic modulus. The Lagrangian of the graphene membrane interacting with the electrostatic gate now has the form

$$\mathcal{L} = \frac{\rho}{2} \int dA (\dot{u})^2 - \frac{\sigma}{2} \int dA (\nabla u)^2 - \frac{C}{16} \left(\frac{\int dA (\nabla u)^2}{\int dA} \right) \int dA (\nabla u)^2 + \frac{\epsilon_0 V_{\text{DC}}^2}{2} \int \frac{dA}{d-u}. \quad (3.28)$$

We approximate the solution to $u(\vec{r}, t)$ to have two components, a static displacement and an oscillating component. To second order, the static displacement will have the mode shape $u_0(r) = \left(1 - \left(\frac{r}{a}\right)^2\right)$, which assumes a parabolic deflection due to the back-gate (which is the solution to a stressed circular membrane under constant force). The term oscillating at the fundamental resonance frequency has the approximate mode shape from the membrane equation $u_1(r) = J_0\left(\frac{r}{a}\alpha\right)$. Therefore, we make the simplification that mode shape will have the form,

$$u \approx x_0 u_0(r) + x u_1(r). \quad (3.29)$$

The kinetic energy of the membrane is then given by the integral

$$T = \frac{\rho}{2} \int dA (\dot{u})^2 = \frac{\rho}{2} \dot{x}^2 \int dA (u_1)^2, \quad (3.30)$$

by plugging in the trial solution given in Equation 3.29 into the kinetic energy term. In our system, the displacements are small compared to the size of the cavity, so that to $x, x_0 \ll d$ and so we can expand the bias voltage term throwing out terms in $\left(\frac{u}{d}\right)^3$ and higher. Performing this expansion, we find the capacitive energy term simplifies to

$$E_C = \frac{\epsilon_0 V^2}{2} \int \frac{dA}{d-u} \approx \frac{\epsilon_0 V_{\text{DC}}^2}{2d} \int dA \left(1 + \frac{u}{d} + \frac{u^2}{d^2}\right). \quad (3.31)$$

Next, we expand these terms according to Equation 3.29

$$E_C \approx \frac{\epsilon_0 V_{\text{DC}}^2}{2d} x \left(\int dA u_1 + \frac{2x_0}{d^2} \int dA u_0 u_1 \right) + \frac{\epsilon_0 V_{\text{DC}}^2}{2d^3} x^2 \int dA u_1^2 + \text{const}, \quad (3.32)$$

where we group all terms in terms of x . The potential energy due to initial in-plane stress can be written in the same way so that

$$U_\sigma = \sigma x_0 x \int dA (\nabla u_1)(\nabla u_0) + \frac{\sigma}{2} x^2 \int dA (\nabla u_1)^2 + const. \quad (3.33)$$

The self-stress term has can also be expanded,

$$U_Y = \frac{C}{16} \left(\frac{\int dA (\nabla u)^2}{\pi a^2} \right) \int dA (\nabla u)^2 \quad (3.34)$$

$$U_Y = \frac{C}{\pi a^2 16} \left(x^2 x_0^2 \left(2 \int dA (\nabla u_0)^2 \int dA (\nabla u_1)^2 + 4 \int dA (\nabla u_1)(\nabla u_0) \right) \right. \\ \left. + 4 x x_0^3 \int dA (\nabla u_0)^2 \int dA (\nabla u_1)(\nabla u_0) \right) + const + O(x^3), \quad (3.35)$$

where we also drop terms of order x^3 and higher.

The constants terms represent a constant offset in energy, which is independent of the amplitude of vibration. Any terms of order x^3 or higher have been dropped for small amplitude vibrations, because the graphene resonators are always driven with small amplitudes. Altogether, the Lagrangian can be written as

$$L \approx \frac{\rho}{2} \mathbb{I}_{11} \dot{x}^2 - \frac{1}{2} \left(\left(\sigma + \frac{C x_0^2}{4\pi a^2} \mathbb{K}_{00} \right) \mathbb{K}_{11} + \frac{C x_0^2}{2\pi a^2} \mathbb{K}_{10}^2 - \frac{\epsilon_0 V^2}{d^3} \mathbb{I}_{11} \right) x^2 \\ - \left(\left(\left(\sigma + \frac{C x_0^2}{4\pi a^2} \mathbb{K}_{00} \right) \mathbb{K}_{10} \right) x_0 - \frac{\epsilon_0 V^2}{2 d^2} \left(\mathbb{I}_1 + \frac{2x_0}{d} \mathbb{I}_{10} \right) \right) x, \quad (3.36)$$

where \mathbb{I} and \mathbb{K} are defined by the integrals,

$$\mathbb{I}_0 = \int dA u_1 = \frac{2\pi a^2}{\alpha} J_1(\alpha), \quad (3.37)$$

$$\mathbb{I}_{11} = \int dA (u_1)^2 = \pi a^2 J_1(\alpha)^2, \quad (3.38)$$

$$\mathbb{I}_{10} = \int dA u_1 u_0 = \frac{4\pi a^2}{\alpha^2} J_2(\alpha), \quad (3.39)$$

$$\mathbb{K}_{00} = \int dA (\nabla u_0)^2 = 2\pi, \quad (3.40)$$

$$\mathbb{K}_{10} = \int dA (\nabla u_1 \nabla u_0) = 4\pi J_2(\alpha), \quad (3.41)$$

$$\mathbb{K}_{11} = \int dA (\nabla u_1)^2 = \pi \alpha^2 J_1(\alpha)^2. \quad (3.42)$$

Next, we use the Euler-Lagrange equation to find the equations of motion for the amplitude of vibrations x

$$\frac{d}{dt} \left(\frac{\partial L}{\partial \dot{x}} \right) - \frac{\partial L}{\partial x} = 0, \quad (3.43)$$

where we find the equation of motion

$$\begin{aligned} \rho \mathbb{I}_{11} \ddot{x} + \left(\left(\sigma + \frac{C x_0^2}{4\pi a^2} \mathbb{K}_{00} \right) \mathbb{K}_{11} + \frac{C x_0^2}{2\pi a^2} \mathbb{K}_{10}^2 + \kappa \mathbb{J}_{11} - \frac{\epsilon_0 V^2}{d^3} \mathbb{I}_{11} \right) x \\ = \left(\sigma + \frac{C x_0^2}{4\pi a^2} \mathbb{K}_{00} \right) x_0 \mathbb{K}_{10} + \kappa x_0 \mathbb{J}_{10} - \frac{\epsilon_0 V^2}{2 d^2} \left(\mathbb{I}_1 + \frac{2x_0}{d} \mathbb{I}_{10} \right). \end{aligned} \quad (3.44)$$

This equation of motion can be cast into the form of the simple harmonic oscillator by equating the constants in this equation to match $\ddot{x} + \omega^2 x = 0$, which gives the coupled equations

$$\omega^2 = \left(\frac{\sigma}{\rho} + \frac{C x_0^2}{4\pi a^2 \rho} \mathbb{K}_{00} \right) \frac{\mathbb{K}_{11}}{\mathbb{I}_{11}} + \frac{C x_0^2}{2\pi a^2 \rho} \frac{\mathbb{K}_{10}^2}{\mathbb{I}_{11}} - \frac{\epsilon_0 V^2}{d^3 \rho}, \quad (3.45)$$

and

$$\left(\left(\sigma + \frac{C x_0^2}{4\pi a^2} \mathbb{K}_{00} \right) \mathbb{K}_{10} \right) x_0 - \frac{\epsilon_0 V^2}{2 d^2} \left(\mathbb{I}_1 + \frac{2x_0}{d} \mathbb{I}_{10} \right) = 0. \quad (3.46)$$

By plugging in the \mathbb{I} and \mathbb{K} integral solutions we simplify Equations 3.45 and 3.46 to be

$$\omega^2 = \frac{\sigma \alpha^2}{\rho a^2} - \frac{\epsilon_0 V^2}{\rho d^3} + \frac{Y}{a^4 \rho (1 - \nu^2)} x_0^2 \left(\frac{1}{2} \alpha^2 + 8 \left(\frac{J_2(\alpha)}{J_1(\alpha)} \right)^2 \right), \quad (3.47)$$

$$\frac{\epsilon_0 V^2 a^4 J_1(\alpha)}{4 d^2 \alpha J_2(\alpha)} - \frac{Y}{2(1 - \nu^2)} x_0^3 = \left(\sigma a^2 - \frac{4\pi a^4 \epsilon_0 V^2}{\alpha^2 d^3} J_2(\alpha) \right) x_0. \quad (3.48)$$

These coupled equations can be further simplified for lower bias gate voltages such that $x_0 \ll a, d$. In this limit, the static displacement, x_0 , can be solved in Equation 8 to find

$$x_0 \approx \frac{\epsilon_0 V^2 a^2}{8 d^2 \sigma}. \quad (3.49)$$

This approximation for the static displacement can be plugged into Equation 3.47 to find the resonance frequency, where

$$\omega^2 = \frac{\sigma \alpha^2}{\rho a^2} - \frac{\epsilon_0 V^2}{\rho d^3} + \frac{C \epsilon_0^2 V^4}{0.143 \rho d^4 \sigma^2}. \quad (3.50)$$

Fitting the experimental data of $\omega(V_{DC})$ for an 8 μm diameter drumhead according to Equation 3.50 yields the parameters ρ , Y , and σ . Using the data for the shown in Figure 3, we extract $\sigma = 0.1 \text{ N m}^{-1}$, $\rho = 7.5 \times \rho_g$, and $Y = 110 \text{ N m}^{-1}$, where ρ_g is the intrinsic mass density of monolayer graphene ($\sim 7.7 \times 10^{-7} \text{ kg m}^{-2}$). The amount of contaminating mass observed in this device is consistent with other graphene nanomechanical systems that used a polymer transfer technique to suspended graphene sheets^{19,33}.

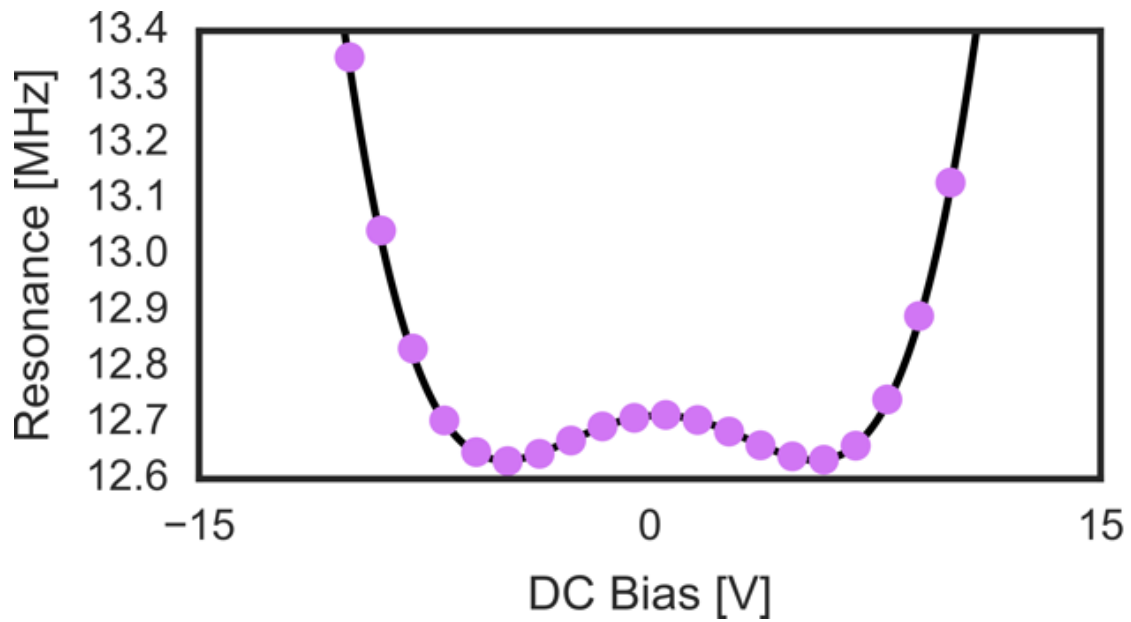


Figure 3.4: The resonance frequency plotted vs. bias voltage (V_{DC}) for an 8 μm diameter drumhead. To extract the resonance frequencies, amplitude-frequency response curve data was fit using damped driven oscillator at varying gate voltages. Using these values, the mass density, initial stress, and elastic modulus were extracted.

CHAPTER IV

GRAPHENE ELECTROMECHANICAL THERMAL DETECTORS

This chapter contains published co-authored material; it has been adapted from Andrew Blaikie, David Miller, and Benjamín Alemán, “A fast and sensitive room-temperature graphene nanomechanical bolometer” *Nature Communications* (2019). In this work, I contributed to the conception and design of the experiments, development of the modelling, the fabrication the graphene devices, the design and construction of the optical measurement apparatus, and the writing of the manuscript. I performed the experiments and analyzed the data.

4.1. Introduction

The bolometer is an essential tool used to detect massive energetic particles and electromagnetic radiation. A primary benefit of the bolometer is its ability to detect light deep into the infrared³⁴, an ability which has advanced thermal imaging, night vision, infrared spectroscopy, and observational astronomy³⁵. Emerging applications³⁶ in scientific imaging, security, remote environmental monitoring, THz communication, solar probes, and communication coupled with the need for increased portability demand that future bolometers work at room temperature and push the limits of speed (bandwidth) and sensitivity (i.e. noise-equivalent power) while also maintaining a large spectral bandwidth. A common method to modify the speed and sensitivity is to change the thermal resistance between the bolometer and its environment³⁴. However, both the

speed and sensitivity are inversely proportional to the thermal resistance, so a sensitive bolometer is often slow.

The speed-sensitivity trade-off can be evaded by decreasing the bolometer heat capacity, since the speed is also inversely proportional to heat capacity. Being just one atom in thickness, graphene offers a tantalizing prospect for ultrasensitive and ultrafast bolometry⁸ because it has the lowest possible heat capacity per unit area of any material. Moreover, graphene possesses an ultra-broadband spectral absorbance^{3,4} and is thermally stable up to at least 2600 K (ref. ²²), so a graphene bolometer could detect electromagnetic radiation of nearly any wavelength and withstand high operating temperatures. However, graphene has performed poorly in conventional bolometry³⁷—where the electrical resistance serves as the readout for absorbed power—because its electrical resistivity is relatively insensitive to temperature³⁸. While graphene has shown promise in hot electron bolometry^{9–13}, in which a weak electron-phonon interaction generates a thermally insulated electron gas with a low electronic heat capacity, these implementations require cryogenic temperatures and lack portability.

Here we pursue an alternative to electrical bolometry and develop a graphene nanomechanical bolometer (GNB). In nanomechanical bolometry³⁹, absorbed power is measured by monitoring changes in a miniaturized mechanical structure, like the deflection of a microbeam⁴⁰. In our GNB (illustrated in Figure 4.1a), we measure the resonance frequency of a mechanical resonator³⁹ comprised of a suspended graphene membrane (Figure 4.1b,c). When the temperature of the suspended membrane increases, the stress changes according to the stress-strain relation, $\Delta\sigma = -(\alpha \Delta T) \frac{Y}{1-\nu}$, where Y is the in-plane Young's modulus, σ is the in-plane stress, ν is the Poisson ratio, ΔT is the

temperature change, and α_T is the thermal expansion coefficient⁴¹, which is negative for graphene for the temperature range used in our experiments. Upon absorbing light, the membrane's temperature increases and the resulting thermomechanical stress shifts the resonance frequency^{24,33} by an amount

$$\Delta f_0 = \frac{\alpha}{2\pi a} \sqrt{\frac{(\sigma + \Delta\sigma)a^2}{\rho} + \frac{\kappa\alpha^2}{\rho}} - f_0 \approx f_0 \left(\frac{a^2\Delta\sigma}{2\sigma a^2 + 2\alpha^2\kappa} \right), \quad (4.1)$$

$$\Delta f_0 = f_0 \left(\frac{a^2\alpha_T \left(\frac{Y}{1-\nu} \right)}{2\sigma a^2 + 2\alpha^2\kappa} \right) \Delta T \approx f_0 \left(\frac{\alpha_T Y}{2\sigma(1-\nu)} \right) \Delta T, \quad (4.2)$$

where f_0 is the initial frequency, ρ is the mass per unit area, $\alpha \sim 2.404$ is the membrane constant, a is the radius, and κ is the bending stiffness. In the membrane limit, where $\kappa \ll \sigma a^2$, the frequency shift can be approximated according to Equation 4.2. For typical graphene nanomechanical resonators^{30,41}, a $\Delta T \sim 100$ mK will shift the frequency by a full linewidth, a sizable amount which is readily measured. For a given absorbed power (P_{abs}), the ΔT is amplified by the thermal resistance (R_T), as determined by Fourier's law $\Delta T = P_{\text{abs}} R_T$. The R_T of suspended graphene is abnormally large⁴², but to enhance R_T further, we patterned the suspended graphene²⁰ into a trampoline geometry^{43,44} with narrow, tapered tethers (see Figure 4.1c). This configuration lets us use the low C of graphene and increase R_T , while providing an effective and sensitive means to measure the absorbed light.

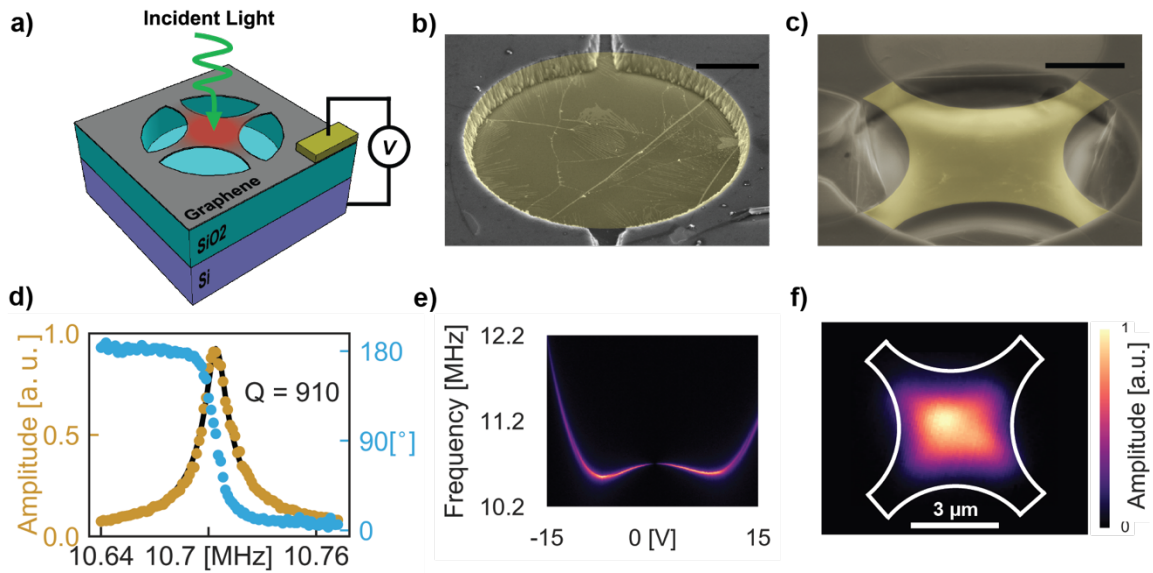


Figure 4.1. Design, images, and mechanical properties of graphene resonators. **a)** Illustration of the bolometric detection scheme. A driving voltage, V_{AC} , is used to actuate motion and a bias voltage, V_{DC} , is used to apply additional tension. The total voltage drop between the suspended graphene and the Si^{++} substrate is $V = V_{DC} + V_{AC}$. Absorbed light tightens the graphene, shifting the mechanical resonance. **b)** False-color scanning-electron-microscope image of a suspended graphene drumhead and **c)** trampoline. Regions of collapsed graphene from the focused ion beam cutting process can be seen around the edges of the cavity. Black scale bars are $2\ \mu\text{m}$. **d)** Amplitude-frequency response curve at $V_{DC} = 0.25\ \text{V}$. The frequency of V_{AC} swept as the mechanical amplitude response is measured. A best fit for a damped driven oscillator is used to calculate the resonance frequency and quality factor. Quality factor is calculated to be $Q = 910$. **e)** Amplitude-frequency spectrogram vs. applied d.c. gate bias. **f)** Measured mechanical mode shape of a graphene trampoline. Fast steering mirrors were used to scan the probe laser across the device with diffraction limited resolution. The white lines are outline the physical device shape as calibrated from a scanning-electron-microscope image. Scale bar is $3\ \mu\text{m}$. Color scale is shared with **e)** and **f)**.

4.2. Description of the GNB fabrication and mechanical measurements

In our GNB, light is detected by tracking changes to the fundamental mode frequency of a graphene nanomechanical resonator. The graphene structures are made by transferring graphene⁴⁵ onto a silicon/silicon oxide support substrate with patterned holes, resulting in circular drumhead resonators (Figure 4.1b). Some drumheads are patterned into trampoline geometries using a focused ion beam technique²⁰, as shown Figure 4.1c. We drive motion of the graphene resonators¹⁸ by applying an a.c. voltage between the graphene and the back-gate (Figure 4.1a), and we measure the motion with a scanning laser interferometer²⁸ operated with a low-power, power-locked laser. By sweeping the a.c. drive frequency, we obtain amplitude and phase spectra, as seen in Figure 4.1d for the first fundamental mode of a trampoline. The resonance frequency can be inferred from either the phase or the amplitude spectrum, which from Figure 4.1d is ~ 10.7 MHz. We obtain the resonance gate dependence by applying a d.c. bias to the graphene while measuring the amplitude spectrum, as shown in Figure 4.1e.

The gate dependence reveals the graphene membrane mass density (ρ), Young's modulus (Y), and initial in-plane stress (σ_0 or tension T), by fitting an electromechanical model on the circular drumhead resonators, which is described in chapter 3. Using the data for a $8 \mu\text{m}$ drumhead, we extract $\sigma_0 = 0.1 \text{ N m}^{-1}$, $\rho = 7.5 \times \rho_g$, and $Y = 110 \text{ N m}^{-1}$, where ρ_g is the intrinsic mass density of monolayer graphene ($\sim 7.7 \times 10^{-7} \text{ kg m}^{-2}$). The amount of contaminating mass observed in this device is consistent with other graphene nanomechanical systems that used a PMMA transfer technique to suspended graphene sheets^{19,33}. We expect that the mass density and modulus of all trampoline and drumhead devices on the chip containing this $8 \mu\text{m}$ drumhead will be the approximately same,

namely $\rho \sim 7.5 \times \rho_g$ and $Y \sim 110 \text{ N m}^{-1}$. However, despite the reduction in clamping perimeter, the trampolines retained a high resonance frequency. Therefore, we expect that the FIB cutting could have significantly increased their in-plane stress.

We track the frequency during light illumination with frequency modulation detection⁴⁶, which uses a phase-locked loop (PLL) with the phase locked on resonance. A key advantage of using frequency modulation is the GNB response bandwidth is not determined by the resonance linewidth, as it is with amplitude modulation detection. The PLL bandwidth allows tracking up to $\sim 50 \text{ kHz}$. For frequency-shift measurements, we maximize the signal-to-noise ratio in several ways. First, we use the scanning interferometer to obtain a two-dimensional spatial map of the vibrational amplitude of the resonator. A map for a trampoline (Figure 4.1f) shows 90-degree rotational symmetry in agreement with the trampoline geometry and goes to zero near the clamping of the tethers indicating they are the only point of contact to the substrate. Using these maps, we position the interferometer laser to maximize the amplitude signal. Moreover, we adjusted the a.c. voltage level to just below the onset of bistability to maximize the resonator amplitude and to avoid nonlinear effects, such as phase instability, which can disrupt the phase-locking.

4.3. Measurement of the noise-equivalent power

The noise-equivalent power ($\text{pW Hz}^{-1/2}$) of the GNB is calculated with the expression $\eta = \sigma_f \sqrt{t} / (f_0 R_f)$, where σ_f is the frequency noise, t is the measurement time, and R_f is the frequency-shift responsivity (i.e. the fractional change in resonance frequency per unit of absorbed power), defined as $R_f \equiv \frac{1}{f_0} \frac{df_0}{dP_{\text{abs}}}$. To determine R_f , we illuminate the GNB membrane with an amplitude-modulated heating laser (532 nm) and

measure f_0 with a PLL. A time recording of f_0 when the GNB is exposed to sinusoidally modulated light is shown in Figure 4.2a, in which $P_{\text{abs}} = 4.4$ nW. Here, we assume the absorption is 2.3% of the incident power^{4,9,11}. The shift Δf_0 is inferred from a sine fit (Figure 4.2a black curve) as the peak-to-peak amplitude. For the data shown in Figure 4.2a, $\Delta f_0 = 8.5$ kHz, corresponding to $\sim 72\%$ of the resonator linewidth. The power dependence of Δf_0 for a trampoline GNB (Figure 4.2b) shows that Δf_0 is linear with P_{abs} (in the range of 1-100 nW) and therefore $\frac{df_0}{dP_{\text{abs}}} = \frac{\Delta f_0}{P_{\text{abs}}}$ is a constant. The linear power dependence of f_0 was observed in all GNB devices. In Figure 4.2c, we plot $R_f = \frac{1}{f_0} \frac{\Delta f_0}{P_{\text{abs}}}$ vs. tether width (w) for 9 different trampolines and 3 different drumheads; for drumheads, w is given by the one-fourth the circumference. The trampoline width (w) is indicated in Figure 4.3b. We tested trampoline GNBs with w ranging from 200 nm to 1.4 μm and GNBs with a d of 6 μm and 8 μm . In general, the drumheads had R_f values about 1% that of trampolines. Our most sensitive device, a 6 μm diameter trampoline with 200 nm wide tethers, had $R_f \sim 300,000$ W⁻¹, a factor 100 greater than state-of-the-art nanomechanical bolometers³⁹. As seen from Figure 4.2c, R_f increases with smaller w for trampolines.

As a measure of the fractional noise, σ_f/f_0 , we used the Allan deviation⁴⁷,

$$\sigma_A^2 = \frac{1}{2(N-1)f_0^2} \sum_{m=2}^N (f_m - f_{m-1})^2, \quad (4.3)$$

where f_m is the average frequency measured over the m th time interval of length t . We calculate σ_A from temporal recordings of the frequency while the heating laser is turned off (Figure 4.2d). Representative Allan deviation data for varying measurement intervals

are presented in Figure 4.2e. Across the sampling range and for all devices, the Allan deviation was flat, taking on a value of $\sim 10^{-5}$, indicating that σ_f is dominated by flicker noise ($1/f$), and not by thermomechanical noise⁴⁸. In this case, the frequency noise is not generally reduced with a larger quality factor^{49,50}.

Combining R_f and the Allan deviation (measured at 100 Hz), we calculate the noise-equivalent power η for each device and plot η vs. w , shown in Figure 4.2f. This data illustrates that η decreases with narrower tether width. A trampoline with a tether width of 200 nm exhibited the best power sensitivity, $\eta = 2 \text{ pW Hz}^{-1/2}$ (at 1 kHz bandwidth), which is also the lowest reported value of noise-equivalent power for a room-temperature graphene bolometer to date¹¹. The η is much larger for drumheads; the largest value ($\eta \sim 1 \text{ nW Hz}^{-1/2}$) is over 200 times greater than the most sensitive trampoline. From these trends, it is clear that reducing the tether width provides a straightforward means to lower, and thus improve, the GNB's η .

Our measurement of η assumes 2.3% absorption. However, cavity effects and surface contaminants could lead to large deviations from 2.3%. Our cavity modelling (see Appendix A) predicts that variations in the absorption are dominated by interference, which changes the overall intensity at the surface of the graphene membrane. For the device geometry used in this work, the intensity, and thus the effective absorption, is reduced to $\sim 0.6\%$. However, surface contaminants on the graphene, which the measured mass density indicates are present, likely increases the total absorption from that predicted from cavity modelling. For the sake of comparison with previous work^{9,11}, we use the standard absorption estimate⁴ of 2.3%.

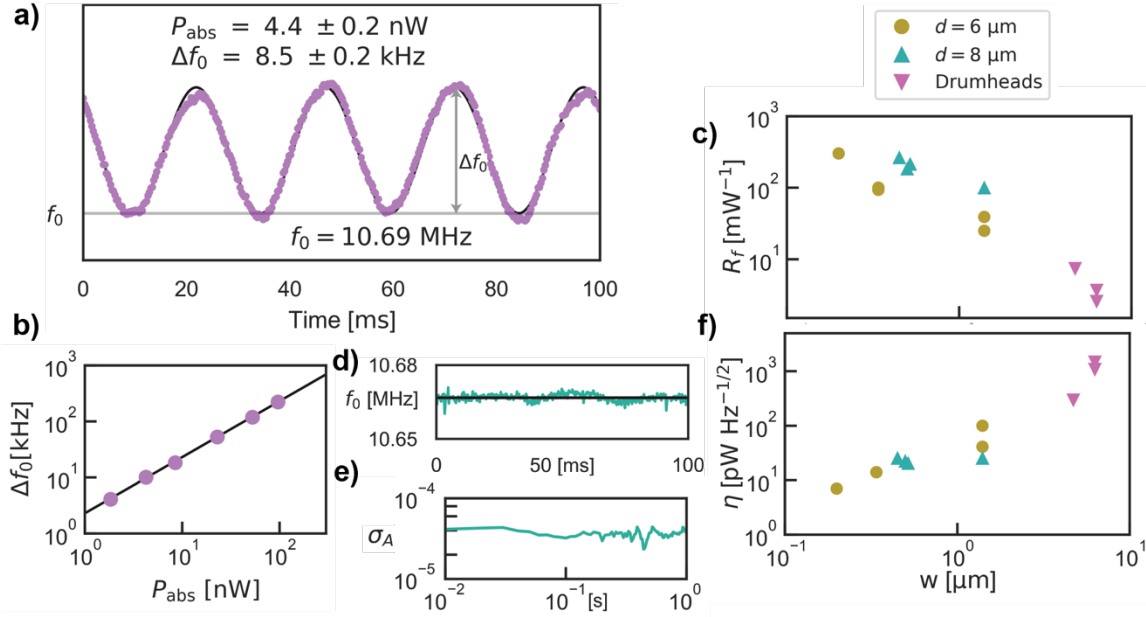


Figure 4.2. Frequency responsivity to absorbed light and frequency noise measurements of graphene resonators. **a)** Mechanical resonance frequency vs. time for a 8 μm diameter trampoline with 500 nm wide tethers. The device is subject to 190 nW of incident radiation modulated at 40 Hz. The absorbed power is $P_{abs} = 4.4$ nW which causes a frequency shift of $\Delta f_0 = 8.5$ kHz. **b)** Measured resonance shift vs. absorbed power. A best-fit line to this data yields a 2.3 kHz nW^{-1} . **c)** Frequency responsivity, R_f , vs. tether width, w , for 9 different trampolines and 3 different drumheads. For the drumheads, the tether width is taken to be 1/4 of the drumhead circumference. **d)** Resonance frequency vs. time for a trampoline GNB device. The device is not exposed with heating laser light other than that needed for the measurement. **e)** Allan deviation, σ_A , of the frequency noise vs. measurement time in a log-log plot. The resonance frequency was tracked with the PLL to obtain temporal frequency data. **f)** Sensitivity, η , vs. tether width for 9 different trampolines and 3 different drumheads. Symbol legend is shared between **c)** and **f)**. Circles indicate a trampoline with a 6 μm diameter, turquoise triangles indicate a trampoline with an 8 μm diameter, and magenta triangles indicate a drumhead resonator of either 6 or 8 μm diameter.

4.4. Modeling of the frequency responsivity to absorbed light.

The observations of R_f and η can be understood through a thermomechanical model that combines a thermal circuit with membrane mechanics. The circuit (shown schematically in Figure 4.3a) treats the GNB as a thermal capacitance C , given by the membrane heat capacity, in parallel with a thermal resistance R_T , governed largely by the tethers (or boundary circumference for drumheads). The absorbed power, $I = P_{\text{abs}}$, obeys the impedance version of Fourier's heat law, $\Delta T = P_{\text{abs}} Z_T$, where ΔT is the temperature difference between the graphene and the surrounding substrate (assumed to be a room temperature thermal ground), and Z_T is the thermal impedance. By using Equation 4.2 and the definition of R_f we can model the frequency responsivity. For an absorbed power modulated at angular frequency ω , the model provides an expression for the frequency-shift responsivity

$$Z_T = \left(\frac{1}{R_T} + \frac{1}{\left(\frac{-i}{\omega C}\right)} \right)^{-1}, \quad (4.4)$$

$$R_f(\omega) = -\frac{\alpha Y}{2\sigma_0(1-\nu)} \frac{R_T}{\sqrt{1 + \omega^2 R_T^2 C^2}}, \quad (4.5)$$

again where α is the thermal expansion coefficient, ν is the Poisson ratio, σ_0 is the initial in-plane stress, and Y is the 2D elastic modulus. We note Equation 4.5 predicts R_f is independent of incident power, in accord the measurements given in Figure 4.2b. In the low-frequency limit (i.e. $\omega \ll \frac{1}{R_T C}$) and with tether resistance $R_T = \frac{\rho_T l}{w}$, where ρ_T is the 2D thermal resistivity of graphene, and l and w are the tether length and width, respectively, Eq. 4.5 simplifies to

$$R_f = \frac{\alpha Y \rho_T}{2 \sigma_0 (1 - \nu)} \frac{l}{w}. \quad (4.6)$$

Measurements of R_f vs. w for trampolines given in Figure 4.2c agree well with Equation 4.6; a fit to $R_f \propto w^{-1}$ for trampolines has a statistical R -value of 0.74. Moreover, the model predicts $\eta \propto w$, which is also in agreement with our measurements (Figure 4.2f; R -value of 0.70). In both cases, the agreement is good despite some variations in σ_0 and l .

4.5. Measurement of the bandwidth.

Another important metric in a bolometer is the response bandwidth, which determines its ability to detect transient signals and fast variations of the radiation intensity. We characterize the bandwidth in two ways. First, we infer the bandwidth (BW) from the 3-dB roll-off of $R_f(\omega)$, which we get by sweeping the modulation frequency, ω , of the heating laser at fixed power and measuring Δf_0 with the PLL and a second lock-in. We fit the measured $R_f(\omega)$ with Equation 4.5 to extract the fit parameter $\tau_T = R_T C$ (*i.e.* the characteristic time of the circuit), thereby obtaining $BW = \sqrt{3}/(2\pi R_T C)$. An R_f spectrum for a trampoline GNB is illustrated in Figure 3c, where the black trace is the fit to Equation 4.5. This spectrum has a nearly flat response, before falling off at $BW \sim 13.8$ kHz. As seen from the fit, the measured $R_f(\omega)$ obeys the circuit model very well.

These spectra provide a direct measure of the BW of R_f , but are limited by the measurement bandwidth of the PLL. To overcome these speed limitations, our second approach infers the BW from the off-resonant thermomechanical out-of-plane displacement of the graphene membrane, which occurs when thermal stress tightens and locally flattens the membrane^{42,51}. In the limit of small displacement and first-order

thermal expansion, the mechanical displacement will be proportional to the change in temperature, $x_0 \propto \Delta T$. Therefore, the mechanical displacement due to a modulated heating laser of frequency ω will obey our thermal circuit model and will have the same frequency dependence as $R_f(\omega)$, as given in Equation 4.5. For these off-resonant measurements, we sweep the modulation frequency of the heating laser at frequencies well below mechanical resonance (in the absence of any electrical actuation) and record the mechanical displacement $x_0(\omega)$. By fitting our measurements of $x_0(\omega)$ to our model, we extract the thermal response time $\tau_T = R_T C$ and thus BW. Figure 4.3d illustrates the real and imaginary parts of $x_0(\omega)$ along with the model fit (black traces) for a trampoline device with $\tau_T = 2.4 \mu\text{s}$ or $\text{BW} = 120 \text{ kHz}$. Where possible, we compared the BW obtained from $R_f(\omega)$ and $x_0(\omega)$, finding excellent agreement, also finding $\text{BW} = 14 \text{ kHz}$ using $x_0(\omega)$ for the device shown in Figure 4.3c. Again, we note that the 3-dB bandwidth is not limited by the mechanical linewidth of the resonator when using frequency modulation⁴⁶. In practice, the BW is limited by either the thermal circuit or PLL bandwidth.

The response bandwidth is strongly correlated with the tether width, where wider tethers produce a faster response. We plot BW vs. w in Figure 4.3e. The BW of trampolines ranged between 10-100 kHz, while for drumheads the BW was as high as 1.3 MHz. For trampolines, our model predicts

$$\text{BW} = \frac{\sqrt{3}}{2\pi c \rho \rho_T l} \frac{w}{A} \quad (4.7)$$

where c is the membrane specific heat, ρ is the membrane mass density, and A is the membrane area. The measured bandwidth data in Figure 4.3e agrees well with the model

prediction $BW \propto w$; for 6 μm diameter trampolines, the linear fit R -value is 0.9. While our experiments did not broadly sample the device area A , our limited data do agree with the prediction $BW \propto A^{-1}$. The BW we measure is likely lower than what we would expect for pristine graphene, as the mass density inferred from the resonance frequency gate dependence is about a factor of ~ 7.5 greater than pristine graphene.

We can estimate the thermal resistance R_T experimentally from the measured thermal time constant τ_T and heat capacity C with the expression, $R_T = \tau_T/C$. The heat capacity for the GNB is $C = (c_g + 6.5c_p)\rho_g \times A$, where the device area is typically ~ 25 - $50 \mu\text{m}^2$, $c_g = 700 \text{ J kg}^{-1} \text{ K}^{-1}$ is the specific heat of graphene, and $c_p \sim 1500 \text{ J kg}^{-1} \text{ K}^{-1}$ is the specific heat of PMMA. For the data shown in Figure 4.3c, $\tau_T = 20 \mu\text{s}$ and $C \sim 2 \times 10^{-13} \text{ J K}^{-1}$ gives $R_T \sim 10^8 \text{ K W}^{-1}$.

The bandwidth and the noise-equivalent power are expected to be directly proportional, regardless of the device geometry. Specifically, our model predicts

$$BW = \left(\frac{\sqrt{3}}{2\pi} \frac{\alpha_T}{\sigma_A \sqrt{t} c \rho} \frac{1}{A} \right) \cdot \eta \quad (4.8)$$

where $\alpha_T = -\frac{\alpha Y}{2\sigma_0(1-\nu)}$ is the frequency coefficient of temperature. In Figure 4.3f we plot BW vs. η , as well as a linear fit to the data (black trace), showing an excellent agreement with the prediction $BW \propto \eta$ (R -value of 0.97). In this data, all parameters are constant except for σ_0 and A , but the larger A devices tend to have lower stress σ_0 so the effects cancel to preserve the linearity. Accordingly, for a given sensitivity, a smaller device area A will boost the speed.

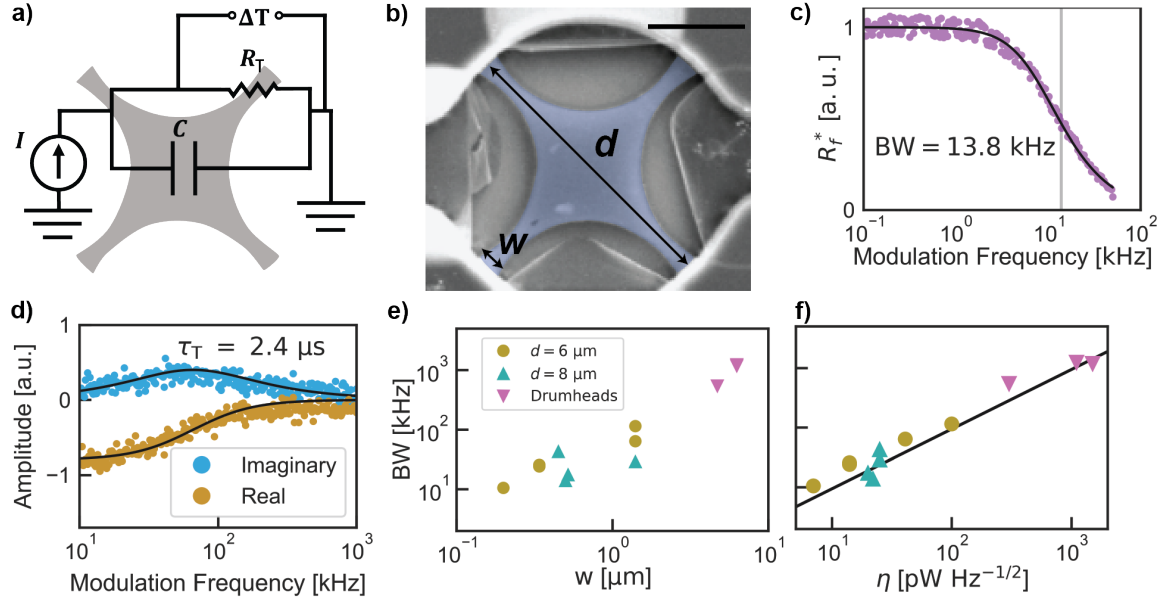


Figure 4.3. Modeling and bandwidth measurements of graphene resonators. **a)** Thermal circuit model. **b)** False-colored scanning electron microscope image of a trampoline of tether width, $w = 200$ nm, and diameter, $d = 6$ μm . Black scale bar is 2 μm . **c)** Normalized frequency-shift responsivity R_f^* as the amplitude of the heating laser is modulated. The total resonance shift reached half its maximum value at $BW = 13.8$ kHz. The fitted curve using Eq. 2 is shown in black. **d)** Amplitude of thermal expansion induced displacement for a trampoline ($w = 1.2$ μm , $d = 6$ μm). The black curve is a fit to the thermal circuit model. From this fit, we extract the thermal response time, $\tau_T = 2.4$ μs . **e)** Bandwidth vs. tether width for 9 different trampolines and 3 different drumheads. For the drumheads, the tether width is taken to be 1/4 of the drumhead circumference. **f)** Sensitivity vs. bandwidth for 9 trampolines and drumheads. The black line is the linear fit (R -value of 0.97). **e)** and **f)** were inferred from the off-resonant thermomechanical method. Symbol legend and vertical axis is shared between **e)** and **f)**. Circles indicate a trampoline with a 6 μm diameter, turquoise triangles indicate a trampoline with an 8 μm diameter, and magenta triangles indicate a drumhead resonator of either 6 or 8 μm diameter.

4.6. Discussion

The response bandwidth and noise-equivalent power demonstrated by our GNB rivals modern high-performance bolometers. Comparing to the sensitivity of previous graphene-based hot-electron bolometers, the GNB is nearly 1000 times more sensitive at room temperature¹¹. Assessing the speed and sensitivity together, our lowest $\eta = 2 \text{ pW Hz}^{-1/2}$ compares favorably to the state-of-the-art in room-temperature bolometry, currently set by vanadium oxide and nickel resistive microbolometers^{52–56} $\sim 1 - 10 \text{ pW Hz}^{-1/2}$, while often outperforming the bandwidth of these systems by several orders of magnitude. Moreover, the drumhead GNBs, though not as sensitive, are $10^3 - 10^5$ times faster than modern vanadium oxide bolometers. Using a standard figure-of-merit (FOM)⁵⁵—which assesses the combination of speed and sensitivity normalized by the device geometry and absorption—we obtain $\text{FOM} = 1.18 \times 10^5 \text{ mK ms } \mu\text{m}^2$, where the best reported FOM values for uncooled microbolometers^{39,52,53,55} are of order $10^5 \text{ mK ms } \mu\text{m}^2$. Thus, despite not yet being optimized and a low optical absorption compared to bulk materials (2.3%), our GNB has already matched these record-low FOM values.

The GNB may enable photodetection applications at very high temperatures because of graphene’s extreme thermal stability. Graphene can sustain temperatures up to at least 2600 K (ref. ²²), and graphene nanomechanical resonators have been shown to operate up to 1200 K (ref. ²³). During our experiments, we tested this thermal stability by irradiating the GNB (as imaged in Figure 4.1c) with a laser power of $\sim 400 \text{ } \mu\text{W}$, a level which we estimate would have increased the GNB temperature as $\Delta T = (\Delta f_0 / f_0) / (R_f / R_T)$. we observed the resonance frequency increase from 10.7 MHz to 35 MHz. Using the measured R_f and R_T for this device, we find $\Delta T \sim 900 \text{ K}$, or $T \sim 1200 \text{ K}$, and

yet the device remained fully operational and undamaged. However, this high temperature probably annealed some of the PMMA contaminating mass as the resonant frequency returned to a higher value after cooling back to room temperature. Although our experiments used a hybrid electronic/optical scheme for actuation and readout, the GNB can be used in an all-optical platform²⁰, eliminating the need for on-chip electronics that could degrade at high temperature. Thus, in contrast with most photodetection technologies, our GNB platform is suitable for relevant high-temperature applications, including safety and security applications like firefighting and industrial process monitoring, and in scientific experiments that take place at high temperature, such as close-proximity solar imaging.

Although we have used the GNB to achieve record bolometric sensitivity at room temperature, it is possible to further improve the noise-equivalent power (η) of our GNB through practical modifications to material properties and device geometry. Our modeling shows that $\eta \propto \sigma$, where σ is stress, so using lower stress graphene⁵⁷ would improve η . Increasing the optical absorption directly improves η to incident power. The GNB absorption could be increased to near unity by placing the bolometer in an optimized optical cavity^{11,39}, at the expense of reduced spectral bandwidth, or by depositing an absorptive material on the GNB, which would also reduce the spectral bandwidth as well as the speed. The simplest way to improve η is to reduce the tether width, which can be narrowed down to ~ 10 nm using FIB (ref. ²⁰), or to use FIB to create lattice defects in the tethers⁵⁸, thereby increasing R_T . Taken together, these changes could bring the noise-equivalent power down to the regime of femtowatt sensitivity with 100 Hz response bandwidth.

The fabrication of the GNB used here is scalable and could be used to make dense bolometer arrays. The process used to make GNB devices involves a single-step transfer of CVD graphene on a lithographically defined resonator support frame, as described in Chapter 2. Graphene transfer and lithography are both routine processing steps in high-yield, large-scale commercial fabrication. Although FIB is not as scalable as optical lithography, modern FIB, much like e-beam lithography, is used in commercial applications. Therefore, GNB trampolines, which only require a fast, single-pass vector cut, could be made quickly and in large numbers. Drumhead GNBs, while not as sensitive as trampolines, do not require FIB shaping and are routinely fabricated in large arrays²⁰, and thus could be especially useful for high-speed applications. Although we operated the GNB with a combination electronic actuation and optical read-out in this work, our GNB could be fully integrated with on-chip electrical detection and actuation^{19,59}, allowing it to operate as a stand-alone, packaged technology.

Sensing is an important application of nanoelectromechanical systems (NEMS). In general, the lower the mass of the NEMS device, the more sensitive it will be. By employing low-dimensional materials (*e.g.* carbon nanotubes and graphene) to operate in the limit of ultralow mass, NEMS sensors have achieved record sensitivity to mass, electrical charge, and force⁶⁰⁻⁶². Our GNB uses an ultralow-mass NEMS device to detect light, and the GNB's high combination of speed and sensitivity is a direct consequence of its small mass and size. The same frequency-shift sensing mechanism that we use to detect optical power will also inherently respond to mass, charge, and force. So, our GNB offers the unique opportunity for multi-mode NEMS sensing, which hybridizes ultrasensitive detection of power with ultrasensitive mass, charge, or force detection.

Using multi-mode sensing, for example, the GNB could simultaneously detect the mass and energy of an incident particle by detecting the transient frequency shift (from the absorbed kinetic energy) and the steady state frequency shift (from the added mass). As consequence of independently measuring the mass and energy of a particle, the GNB would provide a means to measure the momentum of atoms and elementary particles.

In conclusion, we have measured visible light using a graphene nanomechanical resonator by tracking the frequency shifts of the resonator that are induced by light absorption. Using our graphene nanomechanical bolometer (GNB), we achieve a sensitivity of $2 \text{ pW Hz}^{-1/2}$ and a bandwidth up to 1 MHz, thus demonstrating a previously unattainable sensitivity in room-temperature, graphene-based bolometry and greatly outperforming the speed of state-of-the-art room temperature bolometers. By using graphene, we have demonstrated bolometry in the ultimate lower limit of lattice heat capacity and, consequently, have circumvented the speed-sensitivity trade-off that plagues bolometry. Our GNB fills a vital need in portable medical and thermal imaging, THz spectroscopy, and astronomy for fast, sensitive, and spectrally broadband bolometers and bolometer arrays that operate at and far above room temperature. Furthermore, because the GNB detects power via a nanomechanical mechanism, our work opens the possibility of multi-mode NEMS sensing, which may provide a useful tool in material science, nanoscience, and particle physics to simultaneously measure the energy of a particle along with its electrical charge and mass.

4.7. Methods

We fabricated suspended graphene mechanical resonators using standard semiconductor processing techniques as described in Chapter 2. A semi-dry polymer

supported transfer technique was used to place a large sheet of commercial monolayer graphene on Cu foil over the exposed holes and metal contacts. We shaped the graphene into trampolines with a focused ion beam. FIB shaping was performed in an FEI Helios 600i SEM-FIB with a Ga⁺ source. A gallery of scanning electron microscope images of the 12 GNBs characterized in this work is shown in Figure 4.4.

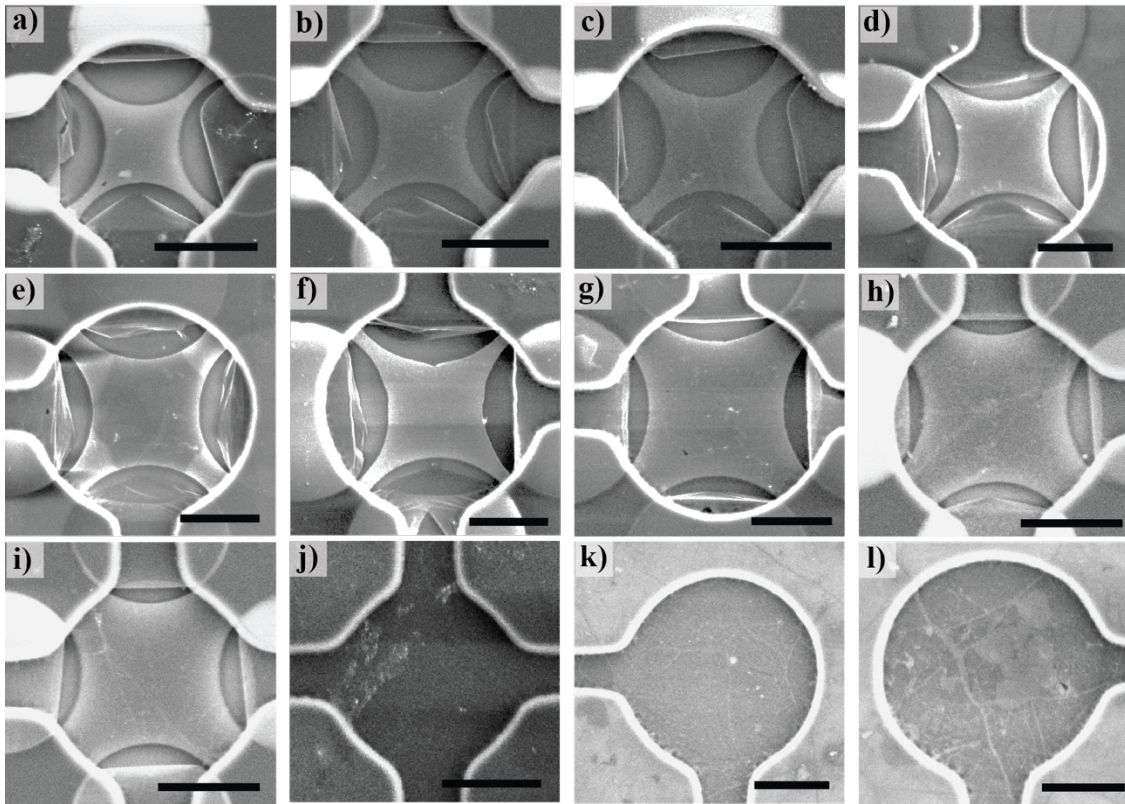


Figure 4.4. SEM images gallery of all devices characterized. Devices are labeled by letters a-l. Devices a-i are trampolines and devices j-l are drumheads. Scale bars are 3 μm .

CHAPTER V

DISSIPATION IN GRAPHENE RESONATORS

This chapter contains unpublished co-authored material; it has been adapted from David Miller[♦], Andrew Blaikie[♦], Brittany Carter, Jayson Paulose, and Benjamín Alemán, “The Role of Wrinkles and Dissipation Dilution in Achieving a High Q factor in Graphene NEMS” *In Preparation* (2020), [♦]Equally contributing author. I contributed to designing the experiments, performing the research, analyzing the data, and writing the manuscript.

5.1. Introduction

In recent years, nanoelectromechanical systems (NEMS) have made significant contributions to many areas of science and technology, from the exquisitely precise detection of temperature⁶³, mass⁶⁰, local forces⁶⁴, and light⁶⁵, to the first tests of coherent quantum mechanics in macroscopic mechanical systems⁶⁶. Future uses for NEMS range from quantum bits, memories and busses to room-temperature neutral-particle mass spectroscopy systems⁶⁷. These uses demand NEMS with an even greater sensitivity and a higher degree of environmental isolation for improved classical⁶⁸ and quantum coherence⁶⁹, which in turn has driven a pursuit for NEMS in the extreme limit of low mass and high mechanical quality factor (Q) (ref. ⁷⁰).

Despite much progress, the quest for both ultralow-mass and high- Q NEMS has fallen short. Silicon-nitride (SiN) beams and membranes possess the highest reported Q , but these bulk structures also have the highest masses, exceeding nanograms (10^{-9} g).

On the extreme end of the mass spectrum are low-dimensional NEMS resonators, such as suspended carbon nanotubes⁷¹ or graphene sheets^{19,59,72}, which possess the lowest-possible mass density (linear or areal) of any material. Graphene NEMS have risen in prominence because of their scalability²⁷, optical addressability⁷³, and large surface-to-volume ratio²⁷, making them particularly ideal for sensing^{21,65} and optomechanical coupling^{74,75,33,42}. Unfortunately, graphene NEMS have been hindered by an extremely low room-temperature Q (ref. ²⁷), typically $Q \sim 10 - 100$.

Efforts to engineer a higher Q have been thwarted by a poor theoretical and experimental understanding of dissipation in graphene NEMS, but there are hints that the Q of graphene membranes can be described by dissipation dilution theory^{44,76-78} (DDT). According to DDT, the Q of a membrane is expected to increase with stress and scale linearly with its lateral size, both which have been observed with graphene drumheads²⁷. In terms of thickness-to-radius aspect ratio ($h/a \sim 10^{-4} - 10^{-5}$), mechanical stress, and elastic modulus, graphene membranes are also physically similar to bulk, three-dimensional (3D) systems that are well-described by dissipation dilution (*e.g.* SiN strings and membranes⁷⁹⁻⁸¹). On the other hand, the DDT for thin plates—the most relevant to graphene membranes—assumes a 3D structure, but experimental measurements of graphene’s elastic properties (in-plane modulus, bending stiffness) often disagree with the 3D model⁸². The predicted thickness-dependence of the Q ($Q \propto h^{-1/2}$) also appears to fail for graphene membranes where Q should be greater than 10,000. Verifying the DDT predictions have been further frustrated by large inconsistencies in the measurements of graphene’s elastic properties—which vary with the measurement method^{31,83}, the level of wrinkling⁸⁴, contamination¹⁹, and strain⁸⁵, and device

fabrication⁸⁶—and because these properties have not been systematically measured and compared to the Q . Altogether, it is unknown if DDT can be appropriately applied to graphene NEMS.

In this work, we show that the Q in suspended graphene drumheads can be understood with a theory of dissipation dilution with a bending stiffness heavily modified by out-of-plane wrinkles. These results demonstrate that out-of-plane wrinkles are responsible for the low Q typically observed in graphene NEMS. A straightforward consequence of this theory is that the application of large amounts of additional in-plane stress is expected to increase the Q by both increasing the elastic energy and reducing wrinkling. To accomplish this, we use Ga^+ irradiation to add high amounts of stress⁸⁵ to a set of bilayer graphene drumheads, and achieve a record $Q \sim 15,000$ in room-temperature graphene NEMS.

5.2. Predictions of dissipation dilution for a Graphene Drumhead.

To test DDT for graphene NEMS, we first outline the predictions of the theory of dissipation dilution for a wrinkled circular membrane. Dissipation dilution refers to the fundamental observation that thin, highly strained NEMS (*e.g.* strings and membranes) primarily store and lose energy through elongation and bending, respectively, so the Q -factor of these mechanical structures can be increased by maximizing the ratio of the elongational energy to the bending losses. This means that the quality factor can simply be approximated as $Q \approx 2\pi \frac{W}{\Delta W_{\text{bend}}}$. The energy lost per cycle is given⁸⁰ by the area integral

$$\Delta W_{\text{bend}} = \pi \kappa_2 \int (\nabla^2 \mathbf{u})^2 dA, \quad (5.1)$$

where κ_2 is the bending loss energy, and $u(\vec{r})$ is the mode shape amplitude for a clamped circular plate. Likewise, the total energy can also be determined⁸⁰ from

$$W = 2\rho \pi^2 f^2 \int u^2 dA, \quad (5.2)$$

where f is the resonance frequency and ρ is the mass-per-unit-area. The quality factor can then be written as the ratio

$$Q = \frac{4 \pi^2 f^2 \rho \int u^2 dA}{\kappa_2 \int (\nabla^2 u)^2 dA}. \quad (5.3)$$

By plugging in the solution for u given in Equation 3.12 in Equation 5.3, the Q of a circular membrane can be approximated as (see Appendix B for more details)

$$Q_{mn} \approx \frac{Q_0}{\lambda} (1 + \lambda \times \alpha_{mn})^{-1}, \quad (5.4)$$

where λ is the dilution factor, α_{mn} is a constant that depends on the mode number ($\alpha_{01} = 2.404$, $\alpha_{11} = 3.832$, *etc.*) and $Q_0 = \frac{\kappa_1}{\kappa_2}$ is the ratio of the bending energy to bending

losses. The increasing nature of the α_{mn} coefficients captures the higher bending losses that accompany the additional curvature of higher order modes. In Equation 5.4, the

dilution factor is $\lambda = \sqrt{\frac{\kappa_1}{\sigma a^2}}$, where a is the membrane radius and σ is the in-plane stress,

and a lower λ predicts a higher Q -factor. Out-of-plane wrinkles⁸⁴ are predicted to modify the elastic properties (κ and Y) of bare two-dimensional (2D) sheets like graphene,

$$\kappa \sim \sqrt{\kappa_{\text{int}} Y_{\text{int}} \langle z^2 \rangle}, \quad (5.5)$$

$$Y \sim \sqrt{\frac{Y_{\text{int}} \kappa_{\text{int}}}{\langle z^2 \rangle}}, \quad (5.6)$$

where κ_{int} and $Y_{\text{int}} = E_{\text{int}} h$ are the intrinsic bending stiffness and in-plane elastic

modulus, respectively, and $z_{\text{RMS}} = \sqrt{\langle z_{\text{eff}}^2 \rangle}$ is the RMS height profile of the wrinkled

membrane. In the simplest terms, DDT of a wrinkled structure predicts that Q -factor of a wrinkled membrane will increase with larger tension and lateral size and decrease with more wrinkling.

5.3. Fabrication of Bilayer Graphene Drumheads

To test the predictions of dissipation dilution for a wrinkled membrane, we fabricate a large array of CVD graphene drumhead resonators⁴⁵ (see Figure 5.1a-b) with diameters ranging from 4.4 μm to 16 μm . We use commercially transferred bilayer graphene (Graphenea) due to an improved yield of large-area drumheads. These devices are electrostatically actuated with an AC-gate voltage (V_{AC}) with a DC offset (V_{DC}) and the motion is measured with a 633 nm HeNe laser using scanning optical interferometry²⁸, which can resolve the mode shape of the various mechanical modes (see Figure 5.1d). All measurements were performed at room temperature under a vacuum of $P < 10^{-5}$ Torr. The laser power is kept low (typically less than 30 μW) to minimize the effects of photothermal heating and laser induced back-action³³, which can artificially modify the Q . Resonance frequencies and Q are obtained by fitting the characteristic amplitude frequency response curves around $V_{DC} = 0$ V, where Joule losses⁸⁷ are minimized.

The Q -factor of our graphene NEMS are expected to be described by Equations 5.4-5.6 which assumes a wrinkled membrane. We confirm the presence of wrinkles using atomic force microscopy (AFM) and find that as-fabricated bilayer graphene drumheads have $z_{RMS} \sim 5$ nm, much larger than the thickness of bilayer graphene, which can be seen in Figure 5.1e. These wrinkles are expected⁷, perhaps arising during the semi-dry graphene transfer or during fabrication.

In order to explicitly determine the role of wrinkles on the Q -factor in graphene NEMS we vary the wrinkle height. Wrinkles in graphene NEMS can be flattened by applying large amounts of in-plane stress⁸⁸. High amounts of stress have previously been achieved with a pressurized gas, low energy Ar^+ irradiation^{89,90}, or with thermal contraction at high-temperatures^{23,90,91}. Here, we use a standard 30 kV Ga^+ focused ion beam (FIB) to deterministically add stress⁸⁵ to a set of 11.6 μm diameter drumheads, see Figure 5.1c. The origin of this stress could be due to the creation of defects in the graphene sheet. We irradiate each device with a calibrated dose at a perpendicular angle of incidence, from 0.2 – 11.8 $\mu\text{C}/\text{cm}^2$. Beyond this dose, we observe that the drumheads begin to fail and tear along defects and grain boundaries, likely due to a combination of damage from the FIB exposure and the high strain values stressing weak spots in the membrane. In order to confirm that the irradiation has reduced the wrinkles⁸⁸, we calibrate the z_{RMS} with AFM images to Ga^+ dose (Figure 5.1g). We find that this method is able to reduce the wrinkling in graphene NEMS down to the theoretical limit⁷ of 1 nm, shown in Figure 5.1f.

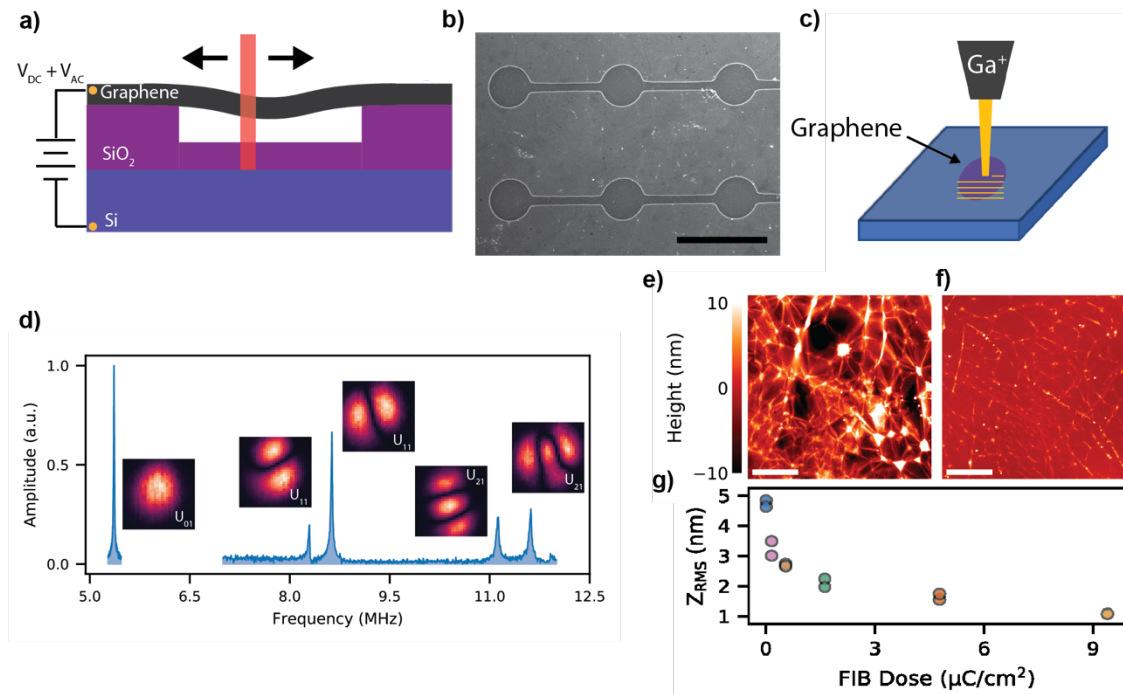


Figure 5.1: Analysis of the bilayer graphene drumhead dataset. (a) Diagram of a graphene NEMS device. (b) Scanning electron microscope image of an array 11.6 μm suspended graphene drumheads. (scale = 20 μm). (c) Diagram of the FIB irradiation process used on some of the 11.6 μm suspended graphene drumheads. (d) Amplitude-frequency response spectra and corresponding mode shapes for the first 5 modes of an 11.6 μm device. (e) AFM image of a non-irradiated bilayer graphene drumhead. (scale = 1 μm). (f) AFM image of a bilayer graphene drumhead irradiated at 4.8 $\mu\text{C}/\text{cm}^2$. (scale = 1 μm). Color scale is shared with e) and f). (g) RMS roughness values at various irradiation doses. Each data point represents the RMS roughness value from 16 μm^2 section of a separate drumhead.

5.4. Characterization of Elastic Parameters

In order to test the dependence of Q to the predictions of DDT, we measure all relevant elastic parameters. First, we measure the device radii a from high resolution scanning electron microscope images. Additional mechanical properties can be extracted from the characteristic resonance frequency-gate voltage dispersion curve, $f_0(V_{\text{DC}})$ (Figure 5.2a). We use a continuum mechanics model^{19,30,33,92} to perform a three-parameter fit to $f_0(V_{\text{DC}})$ to obtain the in-plane stress σ , mass per unit area ρ , and in-plane elastic modulus Y as described in Chapter 3. Values of ρ range between $9 - 11\rho_{\text{g}}$ (where ρ_{g} is the intrinsic mass density of monolayer graphene), which is consistent with bilayer graphene with typical amounts of mass contamination. For the unirradiated drumheads, values of σ vary between 10 and 100 mN m⁻¹ and the average of 4 ± 2 mN m⁻¹. We find that the graphene devices have a modulus of $Y_1 \sim 80$ N m⁻¹, which is consistent with previous work^{30,85} but lower than predicted by the bulk modulus of bilayer graphene, $hE_{\text{graphite}} \sim 670$ N m⁻¹ assuming $h = 0.67$ nm for bilayer graphene. The greatly reduced value of Y is indicative that significant wrinkles are present in the graphene drumheads according to Equation 5.6, which is corroborated with our AFM measurements. The fitting-parameter uncertainty for smaller diameter devices (≤ 7 μm diameter drumheads) was large, so for these diameters we used the average ρ and Y from the larger devices, and we expect this approximation is accurate to within 10% (see Appendix B).

We find that the strain increases super-linearly for the Ga⁺ irradiated devices, as expected by the flattening of the wrinkles, from $\sim .05$ N/m to 1.5 N/m, with FIB dose (Figure 5.2b). Simultaneous to the increase in strain, we also find that that Y increases by

about a factor of 4 (Figure 5.2c) from $\sim 80 \text{ N/m}$ to $\sim 350 \text{ N m}^{-1}$, as has been observed previously in irradiated graphene drumheads^{85,89}. This is much closer to the theoretical value for bilayer graphene of 670 N m^{-1} , which according to Equation 5.6, is predicted to be a consequence of the reduced wrinkling in the membrane.

We are also able to measure the intrinsic bending parameters κ_1 , κ_2 , and $Q_0 = \frac{\kappa_1}{\kappa_2}$, by examining the decrease in quality factor of the higher order modes. We do this by fitting the Q_{mn} vs. mode number to Eq. 5.4 for the first 5 drumhead modes of set of unirradiated $11.6 \mu\text{m}$ graphene drumheads as seen in Figure 5.2d. Using the measured values of λ , T , and a , we then calculate the bending stiffness using $\kappa_1 = a^2 \lambda^2 T$ and find that $\kappa_1 \sim 26 \text{ keV}$, which can be seen in Figure 5.2e. This is a factor of 10^2 larger than predicted by a 3D plate model, where $\kappa_{1,\text{plate}} \approx 160 \text{ eV}$, while the phonon spectrum of graphite⁸⁶ predicts $\kappa_1 \approx 3 \text{ eV}$. However, it is much closer to the value predicted by the $z_{RMS} \sim 5 \text{ nm}$ wrinkle height, which predicts $\kappa_1 \sim 5 \text{ keV}$ (Equation 5.5). A similarly large value of $\kappa_1 \sim 10^3$ has been observed in CVD graphene cantilevers³¹ using non-contact methods. We also fit $Q_0 \sim 50$, as seen in Figure 5.2f. Our measurement of the intrinsic quality factor is in line with an extrapolation of the thickness-dependent quality factor seen in SiN strings^{25,26}, $Q_0 \sim 6900 \frac{h}{100 \text{ nm}}$. Taking the bilayer graphene thickness to be $.67 \text{ nm}$, we expect $Q_0 \sim 47$, in excellent agreement with our fits. This intrinsic dissipation is thought to arise from surface losses that are ubiquitous to various thin NEMS²⁵.

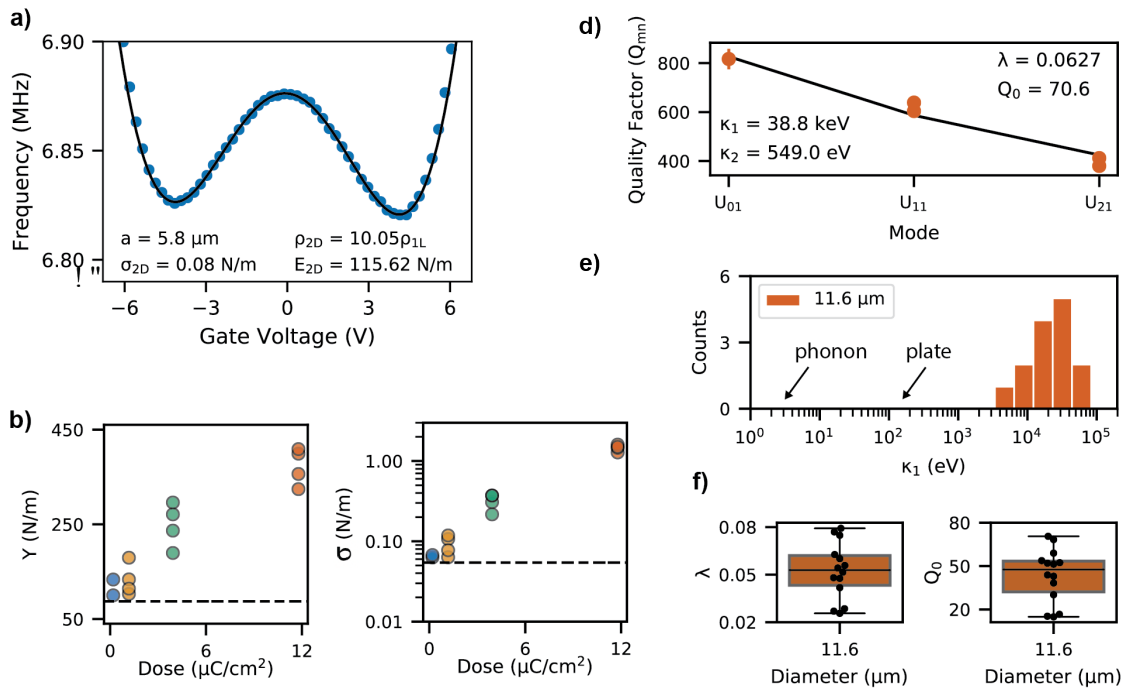


Figure 5.2: Elastic properties of the bilayer graphene drumheads. (a) Resonance frequency of a 11.6 μm bilayer graphene drumhead as the gate voltage is swept from −6 V to 6 V. The black line is the fit to the data which gives mechanical parameters of $\sigma_{2D} = .08 \text{ N/m}$, $\rho_{2D} = 10.05 \rho_{1L}$, and $E_{2D} = 115.62 \text{ N m}^{-1}$. (b) σ vs. Ga⁺ dose for the irradiated 11.6 μm bilayer graphene drumheads. (c) Y vs. Ga⁺ dose for the irradiated 11.6 μm bilayer graphene drumheads. The black line in b-c indicates the average value for non-irradiated drumheads of the same diameter. (d) Q as a function of mode number for an 11.6 μm diameter device. Fitting yields $Q_0 = 70.6$, $\lambda = 0.0627$, $\kappa_1 = 38.8 \text{ keV}$, and $\kappa_2 = 549 \text{ eV}$. (e) Q_0 and λ derived from the fit shown in d for a number of 11.6 μm diameter drumheads. (f) Logarithmic histogram of measured κ_1 values for 11.6 μm drumheads.

5.5. Comparison to Dissipation Dilution Theory

Broadly, the quality factors of our graphene NEMS devices agree with the theory of dissipation dilution. First, we observe a size-dependent quality factor in the unirradiated drumheads (Figure 5.3a), ranging from $Q \sim 400$ for 4.4 μm diameter drumheads to $Q \sim 1600$ for the largest 16.6 μm diameter devices, in accord with previous work on graphene membranes^{27,81}. Another straightforward prediction of DDT is that the Ga^+ irradiated devices should have the largest Q , because of their larger in-plane stress. In accord this prediction, we see a dramatic increase in the quality factor for the irradiated drumheads. In fact, Q_{01} increases by a factor of $\sim 15 - 20$, from $Q \sim 700$ for non-irradiated drumheads to nearly $Q \sim 15,000$ at 11.8 $\mu\text{C } \mu\text{m}^{-2}$ (Figure 5.3b), which is the highest reported quality factor in graphene NEMS at room-temperature to date (Figure 5.3c).

As a further test of DDT, these Ga^+ irradiated devices should have the smallest dilution factor λ . In addition to a higher Q , a small λ also makes predictions about the quality factors of the higher order modes, which can be tested independently. According to Equation 5.4, the ratio of the first higher order mode to the fundamental mode can be cast into the Q_0 -independent ratio:

$$\frac{Q_{11}}{Q_{01}} = \frac{(1 + \lambda \times (2.404)^2)}{(1 + \lambda \times (3.832)^2)} \rightarrow 1 \quad (\lambda \ll 1), \quad (5.4)$$

which goes to unity for small λ . To test this trend for the Ga^+ irradiated devices, we first measure the amplitude spectrum and then identify the U_{01} and U_{11} modes using scanning optical interferometry²⁸. With the modes identified, we extract Q_{01} and Q_{11} by fitting the spectral peaks and calculate $\overline{Q_{11}}/Q_{10}$ for a number of different Ga^+ ion doses, where $\overline{Q_{11}}$

is the average Q of the degenerate pair of modes, (see Figure 5.3d). In accordance with the prediction, the devices with the largest Ga^+ doses have $\frac{\overline{Q_{11}}}{Q_{10}} \rightarrow 1$.

Finally, we compare the quality factor of the entire suspended graphene drumhead dataset (Ga^+ irradiated and unirradiated) to the predictions of DDT. By expanding Equation 5.4 and solving for z_{RMS} in Equations 5.5 and 5.6, we write the dilution factor for a wrinkled membrane in terms the parameter $\left(\frac{Y}{Y_{\text{int}}}\right) \sigma a^2$,

$$\frac{1}{\lambda} \approx \kappa_{1,\text{int}}^{-\frac{1}{2}} \sqrt{\left(\frac{Y}{Y_{\text{int}}}\right) (\sigma a^2)}. \quad (5.5)$$

We use the measured average of $Q_0 \sim 50$ and use $\kappa_1 \sim 26$ keV with the corresponding $z_{\text{RMS}} \sim 5$ nm and $\kappa_{\text{int}} \sim 160$ eV and to calibrate a scaling constant ~ 4 according to Equation 5.5. Altogether, we plot the Q all of the characterized devices and the theory according to Equation 5.5 against the scaled energy parameter $\left(\frac{Y}{Y_{\text{int}}}\right) \sigma a^2$ (see Figure 5.3e). This dataset spans over ~ 4 orders of magnitude in energy and is in agreement with the theory of dissipation dilution with a bending stiffness heavily modified by out-of-plane wrinkles. Ultimately, this data shows that DDT is relevant to graphene NEMS if the wrinkles are accounted for, and that a practical method to engineer a higher Q in suspended graphene sheets is by reducing wrinkles or increasing the diameter and strain.

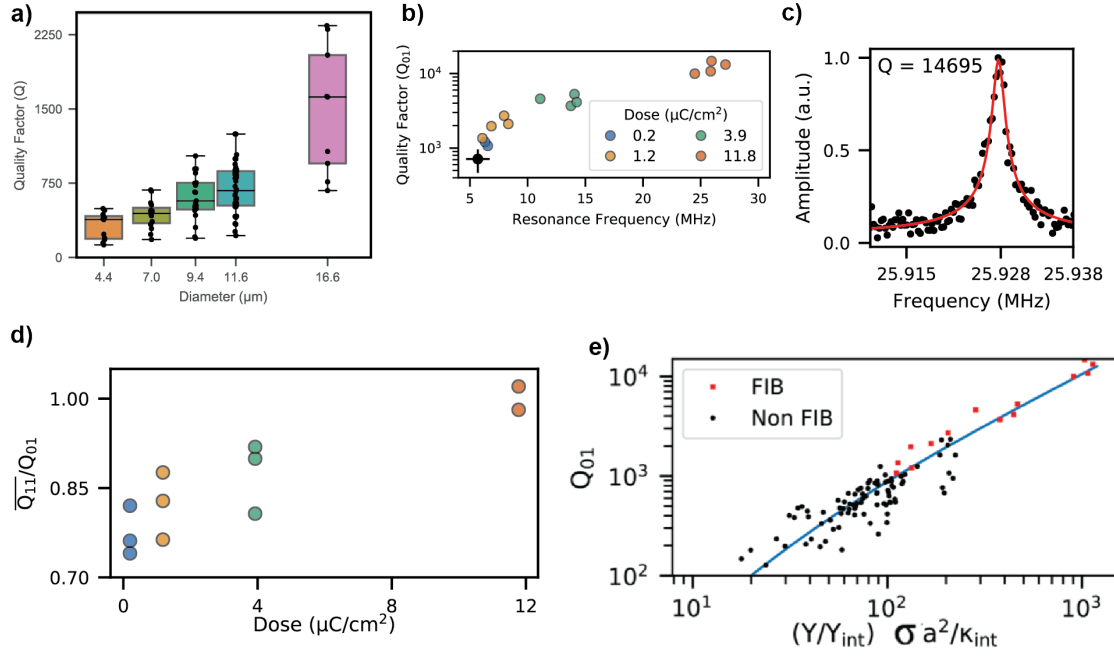


Figure 5.3: Quality factor properties of bilayer graphene drumheads. (a) (b) Q vs. f_0 for the 4 different Ga^+ doses. The black error bars show the mean and standard deviation of the non-irradiated 11.6 μm devices. (c) Amplitude-frequency response curve used to extract the highest quality factor, where $Q \sim 15,000$. (d) $\overline{Q_{11}}/Q_{01}$ vs. FIB dose with the black line again indicating the value for non-irradiated 11.6 μm diameter drumheads. (e) All measured FIB and non-FIB devices with $\kappa_1 = 160$ eV and $Y_{\text{int}} = 670$ N/m. We use the average value of $Y \approx 91$ N/m obtained from the non-irradiated 11.6 μm drumheads for devices where we do not measure Y . The blue line represents a fit to Equation 5.4.

5.6. Discussion

Our results explain the persistently low Q in graphene NEMS. For the stress values and aspect ratios in this work, a much lower dilution factor $\lambda \sim .0017$ is expected in an 11.6 μm diameter unirradiated graphene bilayer drumhead, according to the prediction for the bending stiffness $\kappa_1 = \frac{\gamma h^2}{12(1-\nu^2)}$ in a bulk material, which is a factor of 30 lower than we measure and comparable to mm-size SiN strings and membranes^{80,81}. Even for the relatively low $Q_0 \sim 50$, this small λ predicts room-temperature quality factors of $Q \sim 30,000$, which is much higher than has ever been experimentally observed. Therefore, we propose that an anomalously large bending stiffness, caused by wrinkles, is responsible for the low Q in graphene NEMS. This result likely holds for single-layer 2D NEMS, which will have a somewhat lower value of κ_1 , but a commensurately lower value of Q_0 due to increased surface losses.

It is likely that more aggressive shape and strain engineering approaches would lead to even more impressive quality factors. For example, patterning a phononic shield^{76,77} around the graphene NEMS could suppress the bending at the edge, leading to a modified expression for the quality factor⁷⁷, $Q_{mn} \approx Q_0/(\lambda^2 \alpha_{mn})$. Using the estimated values for the bending stiffness and tension for the maximally Ga^+ irradiated graphene drums, this expression predicts a $Q > 10^6$ and $f \times Q = 10^{13}$, potentially allowing for room-temperature quantum optomechanics with atomically-thin materials⁴⁴ or photothermal cooling³³ of a graphene sheet from room temperature to the quantum ground state. Furthermore, these findings can be readily applied to other resonators made from exfoliated graphene⁷² or other 2D materials⁹³ such as MoS_2 , which share similar

aspect ratios and mechanical parameters, but possess other desirable optical and electronic properties.

In conclusion, we have shown that a general theory of dissipation dilution with a wrinkle-corrected bending stiffness broadly describes the observed quality factors of graphene drumheads in terms, of stress, size, modulus, wrinkle height, and mode number. This wrinkle-corrected bending stiffness was found to be two orders of magnitude larger than predicted from a plate model and is likely responsible for the observed low Q in graphene NEMS. The Ga^+ irradiated drumheads were found to have record Q for room temperature graphene NEMS, due to their increased stress and reduced wrinkles. Graphene drumheads with a high Q and ultra-low mass could open the door to extremely-sensitive force and mass sensing or studies of quantum optomechanics^{33,69} in the two-dimensional regime.

5.7. Methods

Bilayer graphene drumheads were fabricated using standard semiconductor processing methods and utilized a commercial semi-dry transfer provided by Graphenea. Briefly, a CHF_3 reactive ion etch was used to pattern $\sim 0.6 \mu\text{m}$ deep holes into $1 \mu\text{m}$ of thermal oxide grown on degenerately doped silicon. The remaining layer of oxide prevents shorting of graphene devices that have collapsed into the holes. Metal contacts are pre-patterned in the vicinity of the holes and the graphene is placed on top of both the contacts and the holes, forming an array of nanoelectromechanical resonators.

We used optical interferometry to measure the mechanical motion of the graphene resonators at room temperature under vacuum ($<10^{-5}$ Torr). A 633nm HeNe laser was passed through a polarizing beam-splitter and quarter wave-plate to split the reflected

light from the incident beam. The light was focused onto the sample with a 50x, 0.42 NA objective lens. A low-finesse Fabry Perot cavity between the suspended graphene drumhead and the backgated silicon modulates the reflected light. This reflected light was collected with an avalanche photodiode and the voltage was put into a lock-in amplifier referenced to the electrical driving voltage.

AFM images were taken using a Bruker Dimension Icon AFM operating in PeakForce Tapping mode using a $\sim 0.4 \text{ N m}^{-1}$ cantilever and a PeakForce set-point of 1 nN. RMS roughness values were obtained by first applying a 2D plane-fit to the images and then using the roughness function in the NanoScope Analysis software package.

CHAPTER VII

CONCLUDING REMARKS

In this dissertation, we have explored the electromechanics of graphene resonators and their use in thermal detectors. First, we began with a procedure on how to make large arrays of circular graphene resonators. These graphene drumheads can be fabricated on a silicon support substrate and capacitively actuated. We then demonstrated how a focused Ga^+ ion beam could be used to cut the graphene drumheads into a graphene trampoline resonator. We described how the motion of these devices was transduced using a scanning laser interferometer.

Next, using a classical approach, we derived all the relevant equations to describe a capacitively driven suspended graphene drumhead. We began with the full equation of motion that included the energies from bending and stress. We took an in depth look at how a large bias voltage can shift the resonance frequency of a graphene sheet and how this shift is negative for small voltages and positive for large voltages. Furthermore, we showed how this resonant frequency shift can be used to extract mechanical parameters like the mass density, elastic modulus and initial in-plane stress.

Readied with the knowledge of how to construct graphene electromechanical resonators and their relevant physics, we demonstrated an entirely new technological application of graphene electromechanical resonators, namely, thermal detectors. We showed that tracking the resonance frequency shift of a graphene electromechanical resonator can be used to transduce the amount of light incident on the device. This type of detector could allow for sensitive detection of far-infrared light at high speeds, which is not possible with photodiodes, bolometers, or pyroelectric detectors.

Next, we performed experiments to show that the dissipation in graphene NEMS is in fact dominated by bending related losses. Interestingly, we found evidence that wrinkles are responsible for the higher than expected rates of dissipation in graphene electromechanical resonators. Furthermore, we showed that applying large amounts of stress with Ga^+ irradiation was able to dramatically increase the quality factor by both suppressing wrinkles and by adding stress. This work demonstrates that graphene electromechanical resonators can be described with a theory of dissipation dilution with a bending stiffness heavily modified by out-of-plane wrinkles.

Altogether, this research produces both technological and scientific advances in the field of graphene nanomechanics. This work advances the understanding of the dissipation mechanisms in graphene resonators, detailing a guiding theory that can be used to increase the quality factor. We have paved the way for future experiments in graphene electromechanical sensors that require a high Q factor, such as photothermal cooling to the quantum ground state or improved force sensors. This work has highlighted the prominent importance of wrinkles in increasing the bending stiffness of graphene electromechanical resonators, which both reduces the quality factor and sets a fundamental limit to the sensitivity of graphene thermal detectors. By demonstrating that a graphene electromechanical resonator makes a state-of-the-art thermal sensor, we have extended the sensing applications of graphene electromechanical resonators beyond mass, force, and pressure sensing, to include detecting light.

APPENDIX A

Supporting Material for Chapter 4. From Andrew Blaikie, David Miller, and Benjamín Alemán, “A fast and sensitive room-temperature graphene nanomechanical bolometer” Nature Communications (2019).

A.1. Optical Absorption Estimate from Cavity Effects.

The GNB device architecture used in our studies forms a Fabry-Perot cavity. Optical cavity effects due to reflections at interfaces will lead to an optical absorption that is a function of the device dimensions and the wavelength of the absorbed light. We calculate the complex amplitude of the reflected electromagnetic wave from the Si and SiO₂ system at the location of the suspended graphene. Summing over all reflections according to the wave transfer matrix method for calculating transmission and reflection through multilayer media⁹⁴ gives the wave-transfer matrix

$$\mathbf{M} = \mathbf{M}_B(\text{SiO}_2 \rightarrow \text{Si}) \times \mathbf{M}_T(\text{SiO}_2) \times \mathbf{M}_B(\text{vac} \rightarrow \text{SiO}_2) \times \mathbf{M}_T(\text{vac}) \quad (\text{A.1})$$

$$\mathbf{M} = \begin{pmatrix} A & B \\ C & D \end{pmatrix} = \begin{pmatrix} \frac{n_s + n_o}{2n_s} & \frac{n_s - n_o}{2n_s} \\ \frac{n_s - n_o}{2n_s} & \frac{n_s + n_o}{2n_s} \end{pmatrix} \times \begin{pmatrix} e^{-i\frac{2\pi n_o d_o}{\lambda}} & 0 \\ 0 & e^{i\frac{2\pi n_o d_o}{\lambda}} \end{pmatrix} \\ \times \begin{pmatrix} \frac{n_o + 1}{2n_o} & \frac{n_o - 1}{2n_o} \\ \frac{n_o - 1}{2n_o} & \frac{n_o + 1}{2n_o} \end{pmatrix} \times \begin{pmatrix} e^{-i\frac{2\pi d_v}{\lambda}} & 0 \\ 0 & e^{i\frac{2\pi d_v}{\lambda}} \end{pmatrix}, \quad (\text{A.2})$$

where \mathbf{M}_B describes a dielectric boundary reflection and \mathbf{M}_T describes the propagation through a homogeneous medium. We calculate \mathbf{M} by using standard values for the refractive index of SiO₂ and Si ($n_o = 1.5$ and $n_s = 4.14$) and by measuring the thickness

of the oxide layer and the distance between the graphene and the oxide with atomic force microscopy (see Figure 2.3 for schematic displaying d_o and d_v), from which we obtain $d_o = 353$ nm and $d_v = 552$ nm, respectively, and use $\lambda = 532$ nm.

In terms of the wave-transfer matrix components C and D , the amplitude of the complex reflected wave is $u_r = -\frac{C}{D} = (-0.55 + 0.26 i)$. The electric field intensity at the

graphene can be written as the sum of the incident and reflected wave $|u|^2 = |1 + u_r|^2$.

The power absorbed by the graphene can be written as a function of electric field intensity at the graphene because the reflection coefficient of graphene is small ($r \sim 0.01$)³³,

$$\beta = \pi\alpha|1 + u_r|^2 = 0.6\% \quad (\text{A.3})$$

where β is the absorption coefficient. We note that an engineered cavity could be used to enhance the absorption to $\beta = \pi\alpha|1 + 1|^2 = 9.2\%$.

A.2. Photothermal Back-action Frequency Responsivity.

Here we estimate the frequency shift due to photothermal backaction³³.

Depending on the location of the graphene membrane in the optical field of the cavity, this photothermal backaction could either enhance or weaken the GNB thermomechanical responsivity. Our modeling and calculations show that photothermal backaction does not cause a significant frequency shift in a GNB when compared to photothermal tensioning. The effective frequency ω_{eff} and damping Γ_{eff} due to photothermal backaction can be written as³³

$$\omega_{\text{eff}} = \omega_0 \left(1 - \frac{1}{1 + \omega_0^2 \tau^2} \frac{\nabla F}{K} \right)^{\frac{1}{2}} \quad (\text{A.4})$$

$$\Gamma_{\text{eff}} = \Gamma \left(1 + Q\omega_0\tau \frac{1}{1 + \omega_0^2\tau^2} \frac{\nabla F}{K} \right) \quad (\text{A.5})$$

where τ is the thermal response time, $\nabla F = \frac{dF_{\text{pth}}}{dz}$ is the derivative of the photothermal force as a function of displacement (ref. ³³), and $K = m\omega_0^2$ is the effective spring constant. Approximating ω_{eff} with a series expansion, because $\nabla F/K \ll 1$ for low absorbed powers, we obtain

$$\omega_{\text{eff}} \approx \omega_0 \left(1 - \frac{1}{2(1 + \omega_0^2\tau^2)} \frac{\nabla F}{K} \right) = \omega_0 - \frac{1}{2} \left(\frac{\Gamma_{\text{eff}}}{\Gamma} - 1 \right) \frac{\omega_0}{Q\tau} \quad (\text{A.6})$$

Then, the frequency responsivity due to photothermal backaction, given by $R_{f,\text{BA}} = \frac{\omega_{\text{eff}} - \omega_0}{\omega_0 P_{\text{abs}}}$, is the relative change in the effective resonance frequency with respect to absorbed power, is

$$R_{f,\text{BA}} \approx \frac{1}{2} \left(\frac{1}{Q\omega_0\tau} \frac{\Gamma_{\text{eff}}}{\Gamma} - 1 \right) \quad (\text{A.7})$$

In this work, we did not have a back-reflecting mirror to enhance cavity effects.

Therefore, we use the measured results from Ref. ³³ and assume an optimized photothermal backaction setup to estimate the upper limit of the frequency responsivity due to photothermal back-action. We use $\frac{\Gamma_{\text{eff}}/\Gamma - 1}{P_{\text{abs}}} \sim 2 \text{ mW}^{-1}$, $Q \sim 500$, $P_{\text{abs}} \sim P_{\text{inc}} \times 0.023$, $\omega_0 = 2\pi \times 5 \text{ MHz}$, and we estimate $\tau \sim 300 \text{ ns}$ instead of the theoretical estimate provided in Ref. ³³ to account for the slower than theoretically predicted thermal response time in suspended graphene⁴². The $\tau \sim 300 \text{ ns}$ estimate used here is consistent with the thermal response time from our measurements and that of Dolleman et al.⁴² Altogether, we estimate $R_{f,\text{BA}} \sim 10^2 \text{ W}^{-1}$ for a 10-micron drumhead with a back-reflecting mirror.

Therefore, the change in frequency due to photothermal back-action, even assuming a perfect reflecting back mirror, is a factor of $10^2 - 10^4$ lower than direct photothermal tensioning (see Supplementary Table 1 for R_f .) Moreover, because for a given absorbed power and displacement the device heats up to a higher temperature resulting in a larger photothermal force—and thus $\nabla F \propto R_T$ —any enhancement to ∇F due to an increased R_T would be canceled by an increase in thermal response time, where $\tau \propto R_T$.

Consequently, the trampolines, which possess a larger R_T , would see little if any enhancement in photothermal backaction when compared to the drumheads.

APPENDIX B

Supporting material for chapter 5. From David Miller[♦], Andrew Blaikie[♦], Brittany Carter, Jayson Paulose, and Benjamín Alemán, “The Role of Wrinkles and Dissipation Dilution in Achieving a High Q factor in Graphene NEMS” *In Preparation* (2020), [♦]Equally contributing author.

B.1. Derivation of Dissipation Dilution for a circular membrane.

The quality factor for a mechanical resonator is defined as $Q = \frac{2\pi W}{\Delta W}$ where W is the total energy and ΔW is the dissipation. When extrinsic losses (such as clamping loss, thermoelastic damping, Joule heating, etc...) are small, the dissipation can be broken into elongational and bending terms, $Q = 2\pi \frac{W}{\Delta W_{elon} + \Delta W_{bend}}$.

In a highly strained NEMS device, $\Delta W_{elon} \ll \Delta W_{bend}$. This means that the quality factor can simply be approximated as $Q \approx 2\pi \frac{W}{\Delta W_{bend}}$. The dissipation is given⁸⁰ by the area integral

$$\Delta W_{bend} = \pi \kappa_2 \int (\nabla^2 u)^2 dA, \quad (B.1)$$

where κ_2 is the bending loss, and u is the mode shape amplitude for a clamped circular plate, which must obey the boundary conditions $\nabla U_{mn}(r = a) = 0$ and $U_{mn}(r = a) = 0$. Likewise, the total energy can also be determined⁸⁰ from the mode shape

$$W = 2\rho \pi^2 f^2 \int u^2 dA, \quad (B.2)$$

where f is the resonance frequency and ρ is the 2D mass density. The quality factor can then be written as

$$Q = \frac{4 \pi^2 f^2 \rho}{\kappa_2} \frac{\int u^2 dA}{\int (\nabla^2 u)^2 dA}. \quad (\text{B.3})$$

For a circular drumhead, we convert to polar coordinates and use a change of variables to simplify Equation B.3 to

$$Q = \frac{4 \pi^2 f^2 \rho}{\kappa_2} \left(\frac{a^2 \int_0^1 \int_0^{2\pi} r u(r, \theta)^2 d\theta dr}{\frac{1}{a^2} \int_0^1 \int_0^{2\pi} r \left(\frac{\partial^2 u(r, \theta)}{\partial r^2} + \frac{1}{r} \frac{\partial u(r, \theta)}{\partial r} + \frac{1}{r^2} \frac{\partial^2 u(r, \theta)}{\partial \theta^2} \right)^2 d\theta dr} \right), \quad (\text{B.4})$$

where f is the resonance frequency of the fundamental mode and a is the radius of the circular membrane. Therefore, to come up with a formula for the quality factor, we only need the mode shape $u[r, \theta]$ and the resonance frequency f_0 . The typical membrane approximation for the mode shape for this calculation is insufficient because significant bending occurs near the clamped region. Instead, we use the full solution for a clamped circular plate²⁹ to get the mode shape

$$u(r, \theta) = A \left(J_n \left(\alpha \frac{r}{a} \right) - \frac{J_n(\alpha)}{I_n(\beta)} I_n \left(\beta \frac{r}{a} \right) \right) \cos(n\theta), \quad (\text{B.5})$$

where J_n is the Bessel function of the first kind, I_n is the modified Bessel function of the first kind, a is the membrane radius, and A is an amplitude normalization parameter (there exists a similar equation with $\sin(n\theta)$ in place of $\cos(n\theta)$). The parameters α and β are determined from the coupled equations

$$\alpha \frac{J_{n+1}(\alpha)}{J_n(\alpha)} + \beta \frac{I_{n+1}(\beta)}{I_n(\beta)} = 0, \quad (\text{B.6})$$

$$\beta^2 - \alpha^2 = \frac{\sigma a^2}{\kappa_1} \stackrel{\text{def}}{=} \frac{1}{\lambda^2}, \quad (\text{B.7})$$

where κ_1 is the bending stiffness, σ is the 2D in plane stress, and λ is defined as the dilation parameter. The first term in Equation B.5, $J_n \left(\alpha \frac{r}{a} \right)$, is the mode shape using the

membrane approximation, and the second, $I_0\left(\beta \frac{r}{a}\right)$ term, adjusts the mode shape to account for the clamped edges. Plugging in the equation for the resonance frequency of a circular plate²⁹, $f = \frac{\alpha}{2\pi a} \sqrt{\frac{\sigma}{\rho}} \left(1 + \frac{\alpha^2 \kappa_1}{a^2 \sigma}\right)^{1/2}$, the complete analytic formula for the quality factor can be written as

$$Q = \frac{\kappa_1 \alpha^2}{\kappa_2 \lambda^2} \frac{(1 + \lambda^2 \alpha^2) \int_0^1 \int_0^{2\pi} r u(r, \theta)^2 d\theta dr}{\int_0^1 \int_0^{2\pi} r \left(\frac{\partial^2 u(r, \theta)}{\partial r^2} + \frac{1}{r} \frac{\partial u(r, \theta)}{\partial r} + \frac{1}{r^2} \frac{\partial^2 u(r, \theta)}{\partial \theta^2} \right)^2 d\theta dr}, \quad (\text{B.8})$$

where Equations 5, 6, and 7 give $u(r, \theta)$.

We assume that $\lambda = \sqrt{\frac{\kappa_1}{\sigma a^2}} \ll 1$, which is expected based on the values of stress, radius, and bending stiffness. With this assumption, we make a few approximations, namely that $\beta \gg 0$, which allows us to assume, $\frac{I_{n+1}(\beta)}{I_n(\beta)} \rightarrow 1$, which then allows us to simplify Equation B.6 to

$$J_n(\alpha) + \frac{\alpha}{\beta} J_{n+1}(\alpha) \approx 0. \quad (\text{B.9})$$

Therefore, since $\beta \gg 0$, we can approximate α is the root of the equation $J_n(\alpha) \approx 0$.

Therefore, we can approximate Equation B.5 as

$$u(r, \theta) \approx A \left(J_n\left(\alpha \frac{r}{a}\right) + \frac{\alpha J_{n+1}(\alpha)}{\beta I_n(\beta)} I_n\left(\beta \frac{r}{a}\right) \right) \cos(n\theta) \quad (\text{B.10})$$

where α is the solution to $J_n(\alpha) = 0$ and β is determined by material parameters $\beta \approx$

$\sqrt{\frac{\sigma a^2}{\kappa_1}} = 1/\lambda$. In the membrane approximation regime $\lambda \ll 1$, the resonance frequency

approaches the membrane approximation $f_0 \approx \frac{\alpha}{2\pi a} \sqrt{\frac{\sigma}{\rho}}$, which we can use to simplify

Equation B.8 to

$$Q = \frac{\kappa_1 \alpha^2}{\kappa_2 \lambda^2} \frac{\int_0^1 \int_0^{2\pi} r u(r, \theta)^2 d\theta dr}{\int_0^1 \int_0^{2\pi} r \left(\frac{\partial^2 u(r, \theta)}{\partial r^2} + \frac{1}{r} \frac{\partial u(r, \theta)}{\partial r} + \frac{1}{r^2} \frac{\partial^2 u(r, \theta)}{\partial \theta^2} \right)^2 d\theta dr}. \quad (B.11)$$

A few assumptions to Equation B.11 can be made by examining the mode shape, Equation B.10. First, for the numerator we approximate the mode shape

$$\int_0^1 \int_0^{2\pi} r u(r, \theta)^2 d\theta dr \approx A \int_0^1 \int_0^{2\pi} r J_n \left(\alpha \frac{r}{a} \right)^2 \cos(n\theta)^2 d\theta dr, \quad (B.12)$$

because the clamping, $I_0 \left(\beta \frac{r}{a} \right)$ term, in Equation B.10 is zero for most of the integral.

Next plug in Equation B.10 into Equation B.11, with the approximation defined in Equation B.12, to obtain

$$Q = \frac{\kappa_1}{\kappa_2} \frac{\alpha^2}{\lambda^2} \frac{\int_0^1 r J_n(\alpha r)^2 dr}{\int_0^1 r \left(\alpha^2 J_n(\alpha r) + \left(\frac{\alpha J_{n+1}(\alpha)}{\beta I_n(\beta)} \right) \beta^2 I_n(\beta r) \right)^2 dr}. \quad (B.13)$$

The cross term in the denominator, $\propto I_n(\beta r) \times J_n(\alpha r)$, can be dropped because there is little overlap between $I_n(\beta r)$ and $J_n(\alpha r)$ over the range of the integral. Dropping this cross term, we simplify Equation B.12 further

$$Q = \frac{\kappa_1}{\kappa_2} \frac{\alpha^2}{\lambda^2} \frac{\int_0^1 r J_n(\alpha r)^2 dr}{\int_0^1 r \alpha^4 J_n(\alpha r)^2 dr + \left(\frac{J_{n+1}(\alpha)}{I_n(\beta)} \right)^2 \int_0^1 r \alpha^2 \beta^2 I_n(\beta r)^2 dr}. \quad (B.14)$$

Solve the integrals to obtain

$$Q = \frac{\kappa_1 \alpha^2}{\kappa_2 \lambda^2} \times \left(\frac{J_{n-1}(\alpha)^2}{\alpha^4 J_{n-1}(\alpha)^2 + \alpha^2 \beta^2 \left(\frac{J_{n+1}(\alpha)}{I_n(\beta)} \right)^2 \left(I_n(\beta)^2 + 2n \frac{I_{n-1}(\beta) I_n(\beta)}{\beta} - I_{n-1}(\beta)^2 \right)} \right). \quad (B.15)$$

Since $\beta \gg 0$, we can utilize the asymptotic approximation,

$$I_n(\beta) \approx \frac{e^\beta}{\sqrt{2\pi\beta}} \left(1 - \frac{4n^2 - 1}{8\beta} \right). \quad (\text{B.16})$$

Using Equation B.16 allows us to simplify the expression by only keeping the terms of highest order in β , where

$$\frac{I_n(\beta)^2 + \frac{2n}{\beta} I_{n-1}(\beta)I_n(\beta) - I_{n-1}(\beta)^2}{I_n(\beta)^2} \approx \frac{1}{\beta}. \quad (\text{B.17})$$

Since $J_n(\alpha) \approx 0$ we can assume that $\left(\frac{J_{n+1}(\alpha)}{J_{n-1}(\alpha)}\right)^2 \approx 1$ by applying the Bessel identity

$nJ_n(x) = \frac{1}{2}x(J_{m-1}(x) + J_{m+1}(x))$. Now the equation for the quality factor can be

written in its most basic form

$$Q = Q_0 \frac{1}{\lambda} (1 + \lambda \alpha^2)^{-1}, \quad (\text{B.18})$$

where $Q_0 = \kappa_1/\kappa_2$ is the ratio of the real to imaginary bending stiffness and is called the intrinsic quality factor.

To compare how well the analytic approximation, Equation B.18, compares with the exact solution, Equations B.5-8, we evaluated the exact solution numerically and compared the results to the analytic solution in Figure B.1. For the values of the dilution factor fitted in this work $\lambda < 0.1$, the analytic approximation has minimal errors when compared to the exact theory.

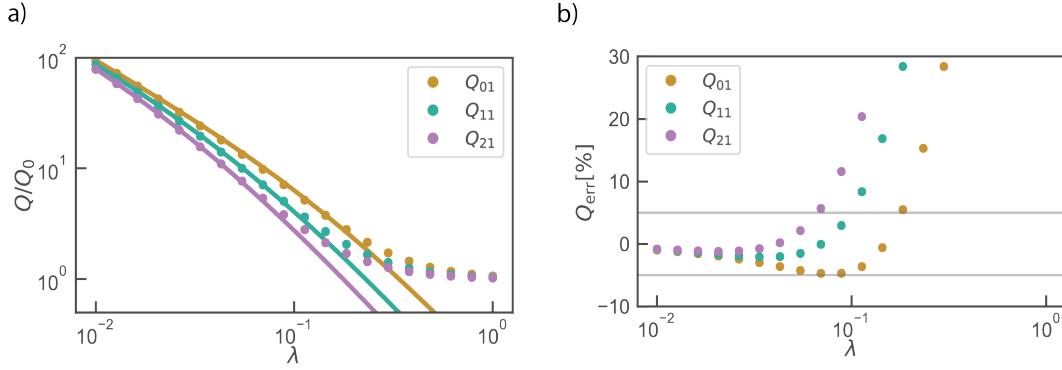


Figure B.1. Dilution factor analytic approximation plotted against the numerical solution. **a)** The real analytic solution is drawn as a solid line and the complete numeric solution is plotted as circles. **b)** The percent error between the analytic solution and the numeric exact solution. For $\lambda < 0.1$ the analytic approximation and the numerical solution have less than 5% error.

B.2. Three-parameter fit method for the frequency-gate response curves.

We find that the robustness of this method is highly dependent on both the shape of the curve (mainly the depth of the local minima) as well as the how large a range of gate voltages are measured (which is often set arbitrarily in previous work). Previous work that used a similar fit found that the theory matched the data only a reasonably low gate voltages³³. One cause of this fitting discrepancy at high voltages is correlations in the parameters of the least-squares fitting function, which become highly correlated when the concave section of $f(V_{DC})$ becomes small compared to the concave up part of the curve. This high fit correlation value leads to diverging values of the fitted parameters and a three-parameter fit method is no longer appropriate. To apply a consistent fitting method across the large dataset of devices, we implement a consistent algorithm.

For these measurements, we perform a non-linear least-squares fit to obtain the best fit the in-plane stress T (previously σ), in-plane modulus Y , and mass per-unit-area ρ for successively larger windows around the mechanical charge neutrality point. We also measure the parameter correlations for each window. We set a cutoff of $\langle Y, \rho \rangle < .95$ and $\langle Y, T \rangle < .95$ and take the last voltage window before this criterion is met and use that as our best fit-parameters. In practice, this turns out to occur at voltages slightly larger than local-minima. Furthermore, we only perform this fit on devices with a large enough radius such that the local-minima dip arising from the $-\frac{\epsilon_0 V_{DC}^2}{d^3 \rho}$ term in Equation 3.50 is prevalent.

The results of this fitting procedure on the graphene drumhead dataset is plotted in Figure B.2. From this data we note several trends, there is large variation, up to 300%, in tension and elastic modulus across the drumheads, see Figure B.2a-b. However, the amount of contaminant mass as determined through this method leads to only a 10% variation, see Figure B.2d-e. This contaminant mass per unit area is relatively consistent across the sample because all drumheads were fabricated using the same polymer transfer. Therefore, by using the average value $\rho_{avg} = 9.64\rho_g$ and the equation for the resonance frequency of a circular membrane, we are able to obtain accurate estimates of the tension, see Figure B.2f.

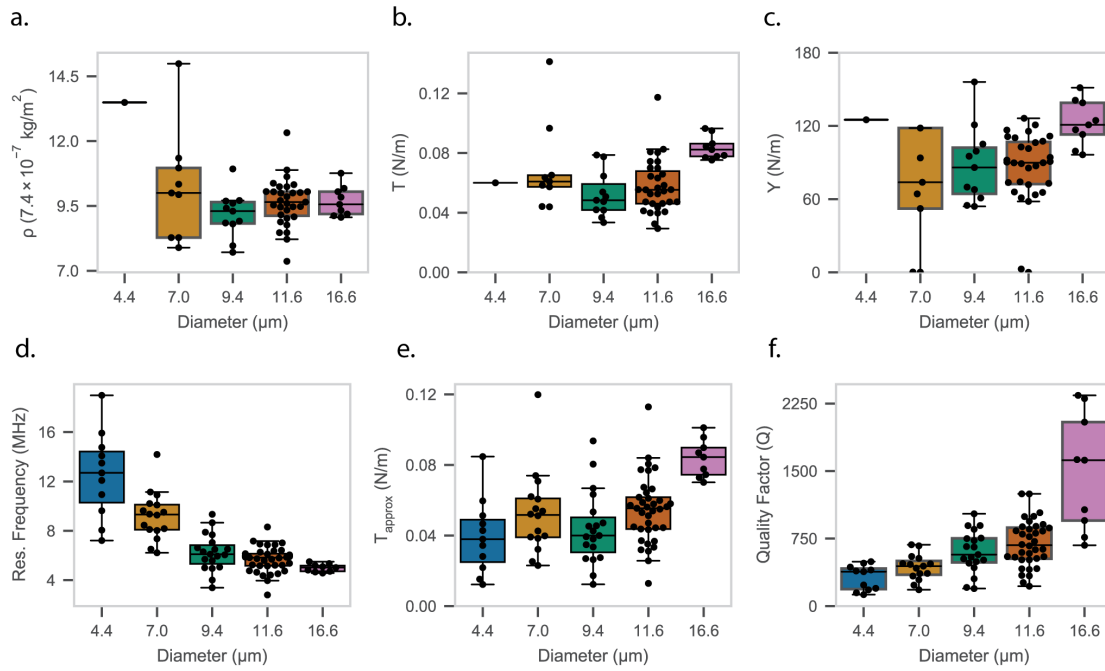


Figure B.2. Elastic properties from 3-parameter fit and approximate value of the mass density. (a-c) Mass density, tension, and 2D modulus vs. diameter obtained directly by fitting the gate-frequency response curves. Outliers for the smaller diameter devices are likely the result of mis-fitting, rather than the true mechanical properties. The average mass density in (b) for the 11.6 μm diameter devices is $\rho_{avg} = 9.64\rho_g \pm .91\rho_g$. (d) Resonance frequency vs. device diameter. (e) Approximate tension vs. device diameter using f_0 and ρ_{avg} . This value of the tension is used throughout the main text rather than those shown in (b). Q vs. device diameter.

REFERENCES CITED

1. Novoselov, K. S. Electric Field Effect in Atomically Thin Carbon Films. *Science* **306**, 666–669 (2004).
2. Lee, C., Wei, X., Kysar, J. W. & Hone, J. Measurement of the elastic properties and intrinsic strength of monolayer graphene. *Science* **321**, 385–388 (2008).
3. Dawlaty, J. M. *et al.* Measurement of the optical absorption spectra of epitaxial graphene from terahertz to visible. *Appl. Phys. Lett.* **93**, 131905 (2008).
4. Nair, R. R. *et al.* Fine Structure Constant Defines Visual Transparency of Graphene. *Science* **320**, 1308 (2008).
5. Mermin, N. D. Crystalline Order in Two Dimensions. *Phys. Rev.* **176**, 250–254 (1968).
6. Landau, L. D. & Lifshitz, E. M. *Statistical Physics Part I.* (Oxford, 1980).
7. Meyer, J. C. *et al.* The structure of suspended graphene sheets. *Nature* **446**, 60–63 (2007).
8. Koppens, F. H. *et al.* Photodetectors based on graphene, other two-dimensional materials and hybrid systems. *Nat. Nanotechnol.* **9**, 780–793 (2014).
9. Yan, J. *et al.* Dual-gated bilayer graphene hot-electron bolometer. *Nat. Nanotechnol.* **7**, 472–478 (2012).
10. El Fatimy, A. *et al.* Epitaxial graphene quantum dots for high-performance terahertz bolometers. *Nat. Nanotechnol.* **11**, 335–338 (2016).
11. Efetov, D. K. *et al.* Fast thermal relaxation in cavity-coupled graphene bolometers with a Johnson noise read-out. *Nat. Nanotechnol.* **13**, 797–801 (2018).
12. Han, Q. *et al.* Highly sensitive hot electron bolometer based on disordered graphene. *Sci. Rep.* **3**, 1–6 (2013).
13. Fong, K. C. & Schwab, K. C. Ultrasensitive and wide-bandwidth thermal measurements of graphene at low temperatures. *Phys. Rev. X* **2**, 1–8 (2012).
14. Bessonov, A. A. *et al.* Compound Quantum Dot-Perovskite Optical Absorbers on Graphene Enhancing Short-Wave Infrared Photodetection. *ACS Nano* **11**, 5547–5557 (2017).
15. Sassi, U. *et al.* Graphene-based mid-infrared room-temperature pyroelectric bolometers with ultrahigh temperature coefficient of resistance. *Nat. Commun.* **8**, 1–10 (2017).

16. Kruse, P. W. *Uncooled Thermal Imaging Arrays, Systems, and Applications*. (SPIE Press, 2001).
17. Shao, Q., Liu, G., Teweldebrhan, D. & Balandin, A. A. High-temperature quenching of electrical resistance in graphene interconnects. *Appl. Phys. Lett.* **92**, 202108 (2008).
18. Bunch, J. S. *et al.* Electromechanical Resonators from Graphene Sheets. *Science* **315**, 490–493 (2007).
19. Chen, C. *et al.* Performance of monolayer graphene nanomechanical resonators with electrical readout. *Nat. Nanotechnol.* **4**, 861–867 (2009).
20. Miller, D. & Alemán, B. Shape tailoring to enhance and tune the properties of graphene nanomechanical resonators. *2D Mater.* **4**, 025101 (2017).
21. Dolleman, R. J., Davidovikj, D., Cartamil-Bueno, S. J., van der Zant, H. S. J. & Steeneken, P. G. Graphene Squeeze-Film Pressure Sensors. *Nano Lett.* **16**, 568–571 (2016).
22. Kim, K. *et al.* High-temperature stability of suspended single-layer graphene. *Phys. Status Solidi - Rapid Res. Lett.* **4**, 302–304 (2010).
23. Ye, F., Lee, J. & Feng, P. X.-L. Electrothermally Tunable Graphene Resonators Operating at Very High Temperature up to 1200 K. *Nano Lett.* **18**, 1678–1685 (2018).
24. Inoue, T., Mochizuki, Y., Takei, K., Arie, T. & Akita, S. Tuning of the temperature dependence of the resonance frequency shift in atomically thin mechanical resonators with van der Waals heterojunctions. *2D Mater.* **5**, 045022 (2018).
25. Villanueva, L. G. & Schmid, S. Evidence of Surface Loss as Ubiquitous Limiting Damping Mechanism in SiN Micro- and Nanomechanical Resonators. *Phys. Rev. Lett.* **113**, 227201 (2014).
26. Fedorov, S. A. *et al.* Generalized dissipation dilution in strained mechanical resonators. *Phys. Rev. B* **99**, 054107 (2019).
27. Barton, R. A. *et al.* High, size-dependent quality factor in an array of graphene mechanical resonators. *Nano Lett.* **11**, 1232–1236 (2011).
28. Davidovikj, D. *et al.* Visualizing the Motion of Graphene Nanodrums. *Nano Lett.* **16**, 2768–2773 (2016).
29. Colwell, R. C., Stewart, J. K. & Arnett, H. D. The vibration of circular plates. *J. Acoust. Soc. Am.* **34**, 275–281 (1962).

30. De Alba, R. *et al.* Temperature-dependence of stress and elasticity in wet-transferred graphene membranes. *J. Appl. Phys.* **123**, 095109 (2018).
31. Blees, M. K. *et al.* Graphene kirigami. *Nature* **524**, 204–207 (2015).
32. Cleland, A. N. *Foundations of Nanomechanics*. (2003).
33. Barton, R. A. *et al.* Photothermal self-oscillation and laser cooling of graphene optomechanical systems. *Nano Lett.* **12**, 4681–4686 (2012).
34. Richards, P. L. Bolometers for infrared and millimeter waves. *J. Appl. Phys.* **76**, 1 (1994).
35. Richards, P. L. & McCreight, C. R. Infrared detectors for astrophysics. *Phys. Today* **58**, 41–47 (2005).
36. Rogalski, A. & Sizov, F. Terahertz detectors and focal plane arrays. *Opto-Electronics Rev.* **19**, 346–404 (2011).
37. Freitag, M., Low, T., Xia, F. N. & Avouris, P. Photoconductivity of biased graphene. *Nat. Photonics* **7**, 53–59 (2013).
38. Tan, Y.-W., Zhang, Y., Stormer, H. L. & Kim, P. Temperature dependent electron transport in graphene. *Eur. Phys. J. Spec. Top.* **148**, 15–18 (2007).
39. Laurent, L., Yon, J.-J., Moulet, J.-S., Roukes, M. & Duraffourg, L. 12-micron-Pitch Electromechanical Resonator for Thermal Sensing. *Phys. Rev. Appl.* **9**, 024016 (2018).
40. Jones, C. D. W. *et al.* MEMS thermal imager with optical readout. *Sensors Actuators, A Phys.* **155**, 47–57 (2009).
41. Yoon, D., Son, Y.-W. & Cheong, H. Negative Thermal Expansion Coefficient of Graphene Measured by Raman Spectroscopy. *Nano Lett.* **11**, 3227–3231 (2011).
42. Dolleman, R. J. *et al.* Optomechanics for thermal characterization of suspended graphene. *Phys. Rev. B* **96**, 165421 (2017).
43. Reinhardt, C., Müller, T., Bourassa, A. & Sankey, J. C. Ultralow-Noise SiN Trampoline Resonators for Sensing and Optomechanics. *Phys. Rev. X* **6**, 021001 (2016).
44. Norte, R. A., Moura, J. P. & Gröblacher, S. Mechanical Resonators for Quantum Optomechanics Experiments at Room Temperature. *Phys. Rev. Lett.* **116**, 147202 (2016).
45. Suk, J. W. *et al.* Transfer of CVD-Grown Monolayer Graphene onto Arbitrary Substrates. *ACS Nano* **5**, 6916–6924 (2011).

46. Albrecht, T. R., Grütter, P., Horne, D. & Rugar, D. Frequency modulation detection using high-Q cantilevers for enhanced force microscope sensitivity. *J. Appl. Phys.* **69**, 668–673 (1991).
47. Allan, D. W. Statistics of Atomic Frequency Standards. *Proc. IEEE* **54**, 221–230 (1966).
48. Cleland, A. N. & Roukes, M. L. Noise processes in nanomechanical resonators. *J. Appl. Phys.* **92**, 2758–2769 (2002).
49. Sansa, M. *et al.* Frequency fluctuations in silicon nanoresonators. *Nat. Nanotechnol.* **11**, 552–558 (2016).
50. Roy, S. K., Sauer, V. T. K., Westwood-Bachman, J. N., Venkatasubramanian, A. & Hiebert, W. K. Improving mechanical sensor performance through larger damping. *Science* **360**, 1203 (2017).
51. Metzger, C., Favero, I., Ortlieb, A. & Karrai, K. Optical self cooling of a deformable Fabry-Perot cavity in the classical limit. *Phys. Rev. B* **78**, 035309 (2008).
52. Endoh, T. *et al.* Uncooled infrared detector with 12 μ m pixel pitch video graphics array. *Proc. SPIE* **8704**, 87041G (2013).
53. Mizrahi, U. *et al.* Large-format 17 μ m high-end VO_x μ -bolometer infrared detector. *Proc. SPIE* **8704**, 87041H (2013).
54. Yang, H. & Rebeiz, G. M. Sub-10-pW/Hz0.5 Uncooled Micro-Bolometer With a Vacuum Micro-Package. *IEEE Trans. Microw. Theory Tech.* 1–8 (2016).
55. Skidmore, G. D., Han, C. J. & Li, C. Uncooled microbolometers at DRS and elsewhere through 2013. *Proc. SPIE* **9100**, 910003 (2014).
56. Rogalski, A., Martyniuk, P. & Kopytko, M. Challenges of small-pixel infrared detectors: A review. *Reports Prog. Phys.* **79**, (2016).
57. Alemán, B. *et al.* Polymer-free, low tension graphene mechanical resonators. *Phys. Status Solidi - Rapid Res. Lett.* **7**, 1064–1066 (2013).
58. Wang, H. *et al.* Experimental study of thermal rectification in suspended monolayer graphene. *Nat. Commun.* **8**, 15843 (2017).
59. Kumar, M. & Bhaskaran, H. Ultrasensitive Room-Temperature Piezoresistive Transduction in Graphene-Based Nanoelectromechanical Systems. *Nano Lett.* **15**, 2562–2567 (2015).
60. Moser, J. *et al.* Ultrasensitive force detection with a nanotube mechanical resonator. *Nat. Nanotechnol.* **8**, 493–496 (2013).

61. Steele, G. a *et al.* Strong coupling between single-electron tunneling and nanomechanical motion. *Science* **325**, 1103–7 (2009).
62. Rugar, D., Budakian, R., Mamin, H. J. & Chui, B. W. Single spin detection by magnetic resonance force microscopy. *Nature* **430**, 329–332 (2004).
63. Larsen, T. *et al.* Ultrasensitive string-based temperature sensors. *Appl. Phys. Lett.* **98**, 121901 (2011).
64. Moser, J. *et al.* Ultrasensitive force detection with a nanotube mechanical resonator. *Nat. Nanotechnol.* **8**, 493–496 (2013).
65. Blaikie, A., Miller, D. & Alemán, B. J. A fast and sensitive room-temperature graphene nanomechanical bolometer. *Nat. Commun.* **10**, 4726 (2019).
66. O’Connell, A. D. *et al.* Quantum ground state and single-phonon control of a mechanical resonator. *Nature* **464**, 697–703 (2010).
67. Dominguez-Medina, S. *et al.* Neutral mass spectrometry of virus capsids above 100 megadaltons with nanomechanical resonators. *Science* **362**, 918–922 (2018).
68. Okamoto, H. *et al.* Coherent phonon manipulation in coupled mechanical resonators. *Nat. Phys.* **9**, 598–598 (2013).
69. Rossi, M., Mason, D., Chen, J., Tsaturyan, Y. & Schliesser, A. Measurement-based quantum control of mechanical motion. *Nature* **563**, 53–58 (2018).
70. Ekinci, K. L. & Roukes, M. L. Nanoelectromechanical systems. *Rev. Sci. Instrum.* **76**, 061101 (2005).
71. Jensen, K., Kim, K. & Zettl, A. An Atomic-resolution nanomechanical mass sensor. *Nat. Nanotechnol.* 533–537 (2008). doi:10.1038/nnano.2008.200
72. Bunch, J. S. *et al.* Electromechanical Resonators from Graphene Sheets. *Science* **315**, 490–493 (2007).
73. Miller, D. & Alemán, B. Spatially resolved optical excitation of mechanical modes in graphene NEMS. *Appl. Phys. Lett.* **115**, 193102 (2019).
74. Weber, P., Güttinger, J., Tsioutsios, I., Chang, D. E. & Bachtold, A. Coupling Graphene Mechanical Resonators to Superconducting Microwave Cavities. *Nano Lett.* **14**, 2854–2860 (2014).
75. Singh, V. *et al.* Optomechanical coupling between a multilayer graphene mechanical resonator and a superconducting microwave cavity. *Nat. Nanotechnol.* **9**, (2014).

76. Tsaturyan, Y., Barg, A., Polzik, E. S. & Schliesser, A. Ultracoherent nanomechanical resonators via soft clamping and dissipation dilution. *Nat. Nanotechnol.* **12**, 776–783 (2017).
77. Ghadimi, A. H. *et al.* Elastic strain engineering for ultralow mechanical dissipation. *Science* **360**, 764–768 (2018).
78. Reinhardt, C., Müller, T., Bourassa, A. & Sankey, J. C. Ultralow-Noise SiN Trampoline Resonators for Sensing and Optomechanics. *Phys. Rev. X* **6**, 021001 (2016).
79. Schmid, S., Jensen, K. D., Nielsen, K. H. & Boisen, A. Damping mechanisms in high-Q micro and nanomechanical string resonators. *Phys. Rev. B* **84**, 165307 (2011).
80. Yu, P. L., Purdy, T. P. & Regal, C. A. Control of material damping in High-Q membrane microresonators. *Phys. Rev. Lett.* **108**, 1–5 (2012).
81. Unterreithmeier, Q. P., Faust, T. & Kotthaus, J. P. Damping of Nanomechanical Resonators. *Phys. Rev. Lett.* **105**, 027205 (2010).
82. Akinwande, D. *et al.* A review on mechanics and mechanical properties of 2D materials — Graphene and beyond. *Extrem. Mech. Lett.* **13**, 42–77 (2017).
83. Wang, G. *et al.* Bending of Multilayer van der Waals Materials. *Phys. Rev. Lett.* **123**, 116101 (2019).
84. Kosmrlj, A. & Nelson, D. R. Mechanical Properties of Warped Membranes. **012136**, 1–12 (2013).
85. Nicholl, R. J. T. *et al.* The effect of intrinsic crumpling on the mechanics of free-standing graphene. *Nat. Commun.* **6**, 8789 (2015).
86. Lindahl, N. *et al.* Determination of the Bending Rigidity of Graphene via Electrostatic Actuation of Buckled Membranes. *Nano Lett.* **12**, 3526–3531 (2012).
87. Will, M. *et al.* High Quality Factor Graphene-Based Two-Dimensional Heterostructure Mechanical Resonator. *Nano Lett.* **17**, 5950–5955 (2017).
88. Nicholl, R. J. T., Lavrik, N. V., Vlassiouk, I., Srijanto, B. R. & Bolotin, K. I. Hidden Area and Mechanical Nonlinearities in Freestanding Graphene. *Phys. Rev. Lett.* **118**, 266101 (2017).
89. López-Polín, G. *et al.* Increasing the elastic modulus of graphene by controlled defect creation. *Nat. Phys.* **11**, 26–31 (2015).
90. Robinson, J. T. *et al.* Graphene Strained by Defects. *ACS Nano* **11**, 4745–4752 (2017).

91. Davidovikj, D., Poot, M., Cartamil-Bueno, S. J., van der Zant, H. S. J. & Steeneken, P. G. On-chip Heaters for Tension Tuning of Graphene Nanodrums. *Nano Lett.* **18**, 2852–2858 (2018).
92. De Alba, R. *et al.* Tunable phonon-cavity coupling in graphene membranes. *Nat. Nanotechnol.* **11**, 741–746 (2016).
93. Castellanos-Gomez, A. *et al.* Single-layer MoS₂ mechanical resonators. *Adv. Mater.* **25**, 6719–6723 (2013).
94. Saleh, B. E. A. & Teich, M. C. *Fundamentals of Photonics*. (2012).